Bulletin of Volcanology (2024) 86:50
https://doi.org/10.1007/s00445-024-01743-7

RESEARCH ARTICLE

When the lava meets the sea: emplacement of the 2–4 ka San Bartolo lava flow field, Stromboli volcano (Italy)

Rasia Shajahan[1,2] · Andrew J. L. Harris[3] · Elena Zanella[1,2] · Lucia Gurioli[3] · Claudio Robustelli Test[1,2] · Sonia Calvari[4] · Lodovico Drovanti[1]

Received: 30 January 2024 / Accepted: 15 April 2024 / Published online: 25 April 2024

Abstract

When a lava flow enters a body of water, either a lake, sea, river or ocean, explosive interaction may arise. However, when it is an 'a'ā lava flow entering water, a more complex interaction occurs, that is very poorly described and documented in literature. In this paper, we analysed the 2–4 ka San Bartolo lava flow field emplaced on the north flank of Stromboli volcano, Italy. The lava flow field extends from ~ 650 m a.s.l. where the eruptive fissure is located, with two lava channels being apparent on the steep down to the coast. Along the coast the lava flow field expands to form a lava delta ~ 1 km wide characterised by 16 lava 'Flow' units. We performed a field survey to characterise the features of lava entering the sea and the associated formation of different components and magnetic measurements to infer the flow fabrics and emplacement process of the lava flow system. We measured the density, porosity and connectivity of several specimens to analyse the effect of lava-water interaction on the content in vesicles and their connectivity and conducted a macroscopic componentry analysis (clast count) at selected sites to infer the character of the eroded offshore segment of the lava flow field and its component flow units. The collected data allowed us to define the main components of a lava delta fed by 'a'ā lava flows, with its channels, littoral units, ramps, lava tubes, and inflated pāhoehoe flows controlled by the arterial 'a'ā flow fronts. The spatial organisation of these components allowed us to build a three-step descriptive model for 'a'ā entering a water. The initial stage corresponds to the entry of channel-fed 'a'ā lava flow into the sea which fragments to form metric blocks of 'a'ā lava. Continued lava supply to the foreshore causes flow units to stall while spreading over this substrate. Subsequent 'a'ā lava flow units ramp up behind the stalled flow front barrier. Lava tubes extending through the stalled flow barrier feed the seaward extension of a bench made of several pāhoehoe flow units.

Keywords Stromboli volcano · Compound lava flow field · Lava delta · Magnetic fabrics

Introduction

Entry of lava into water is a common process occurring at volcanic islands (e.g.Mattox and Mangan 1997; Bosman et al. 2014; Poland and Orr 2014), at effusive centres next to lakes (e.g. Jenks et al. 1989; Obata and Umino 1999; Tucker and Scott 2009) or at volcanoes close to the coastline (Mueller et al. 2000; Mulas et al. 2016). This can result in either the formation of a lava delta with no explosive activity (Moore et al. 1973; Maeno et al. 2016) and/or hydro explosions (e.g.Sheridan and Wohletz 1983; Mattox and Mangan 1997; Fitch and Fagents 2020; Soule et al. 2021; Banerjee and Shen 2023), as well as hydrothermal activity (Dundas et al. 2020). In either case, the entry of lava into the water body and the associated processes, landforms and flow field internal structures are not straightforward to interpret,

Editorial responsibility: L. Pioli

✉ Rasia Shajahan
rasia.shajahan@unito.it

[1] Dipartimento di Scienze della Terra, Università degli Studi di Torino, Torino, Italy

[2] CIMaN-ALP, Centro Interuniversitario di Magnetismo Naturale - Alpine Laboratory of Paleomagnetism, via Luigi Massa 4, 12016 Peveragno, Italy

[3] Laboratoire Magmas et Volcans, Université Clermont Auvergne, CNRS, IRD, OPGC, F-63000 Clermont-Ferrand, France

[4] Sezione di Catania-Osservatorio Etneo, Istituto Nazionale di Geofisica e Vulcanologia, Catania, Italy

because the morphology and extent of the lava delta varies depending on effusion rate, the geometry of the shoreline and of the underlying sea floor (Bosman et al. 2014).

Based on observations of pāhoehoe flows entering the ocean in Hawaii, an ocean entry model has been developed whereby tube-fed pāhoehoe flows initially enter the ocean to cause an explosive interaction between molten lava and sea water (Mattox et al. 1993), which creates a near-shore substrate of blocks (Fitch and Fagents 2020). Lava then extends over this substrate to form a subaerial lava 'bench' (Mattox and Mangan 1997; Fitch and Fagents 2020). With time the bench grows seawards to create a lava delta (Moore et al. 1973; Bosman et al. 2014; Soule et al. 2021). Given that the base of the bench is made of unconsolidated rubble, wave action can easily erode the delta to cause sudden collapse and explosive activity (e.g.Obata and Umino 1999; Skilling 2002; Bosman et al. 2014; Poland and Orr 2014). Deltas can also be formed during entry of 'a'ā lava into the sea, as was the case during the April 2007 eruption of Piton de la Fournaise (Staudacher et al. 2009) or the 2002–2003, 2007 and 2014 eruptions at Stromboli (Lodato et al. 2007; Marsella et al. 2012; Bosman et al. 2014; Di Traglia et al. 2018; Casalbore et al. 2021). However, the case of 'a'ā lava flow entry into a lake, sea or ocean has been far less studied. Three of the few such examples are the 1934–1935 Showa Iwo-jima and the 2014 Nishinoshima eruptions in Japan, both forming new islands (Maeno and Taniguchi 2006; Maeno et al. 2016), or the more recent 2021 Tajogaite eruption in the Canaries (Alonso et al. 2023). The interaction of the lava flow fronts with sea water in both cases resulted in crests and troughs of wrinkles of the flow margins, crease structures and subvertical flow banding (Maeno and Taniguchi 2006; Maeno et al. 2016) very similar to what we have observed at Stromboli on the San Bartolo lava flow field.

In this paper, we use a multidisciplinary approach to study the entry into the Tyrrhenian Sea of the San Bartolo lava flows at Stromboli volcano (Italy) (Fig. 1). Due to the exposure of this delta along a 1-km-wide cliff section (Calvari et al. 2023), it provides an excellent location where entry dynamics, processes and resulting structures can be described to study the lava entering the sea. AMS allows quantitative characterisation of lava flow fabrics even when macro- and micro-field structures are not well developed or absent (Canon-Tapia et al. 1996; Cañón-Tapia and Pinkerton 2000; Cañón-Tapia and Coe 2002; Loock et al. 2008; Sangode et al. 2022. AMS can be used not only to determine flow direction, but also to understand internal lava structures and infer emplacement dynamics (Loock et al. 2008; Prival et al. 2022; Olsanska et al. 2024). In the case of lava flow-water interaction, the lava flow is subject to additional factors as when flowing on land (e.g. thermal gradient between lava and water, water injection velocity and fragmentation). In this case, complex structures develop depending on the degree of water interaction and shoreline (as well as sea floor) topography/geometry. As a result, quantitative analysis of magnetic fabrics provides parameters to facilitate characterisation of such complicated emplacement conditions, allowing us to reconstruct a descriptive sea-entry model for the San Bartolo lava flows.

Geological setting

Stromboli volcano is located on the Aeolian Islands archipelago in the southern Tyrrhenian Sea, off the north coast of Sicily, Italy (Fig. 1b). The volcano is known for its regular explosive eruptions, often involving the emission of bombs and blocks, scoria, lapilli and the release of gas and ash clouds (Chouet et al. 1974; Patrick et al. 2007). It is marked by high K calc-alkaline magmatism, which built up to its present elevation of 924 m over the last 2–5 ka (Francalanci et al. 2013, 2014). The NE flank of Stromboli Island is formed of 11 litho-stratigraphic units from different flank eruptions, with the San Bartolo (SB) lava flow marking the last flank eruption, which occurred outside the Sciara del Fuoco depression (Calvari et al. 2011). The SB lava flow field formed by the monogenetic activity of a NE trending fissure at an elevation of 600–650 m a.s.l. (Fig. 1a) and has an archaeomagnetic age of ~ 2–4 ka (Arrighi et al. (2004); Speranza et al. 2008); thus, it emplaced during the Il Pizzo sequence (Francalanci et al. 2014). Considering this age constraint, when the SB lava emplaced, the sea level was at least 1.35 ± 0.07 m lower than at present, as obtained for the Roman Period on the basis of archaeological constraints (Lambeck et al. 2004). The submerged shelves around the Aeolian Islands are characterised by low-gradient erosive surfaces particularly pronounced along the NE coast of Stromboli (Romagnoli 2013), with a steep seaward shelf break commonly located at depths of 100–120 m below sea level (b.s.l.).

The eruptive fissure, which extends NE and downslope, has a depressed feature in its upper part, indicating that an important drainage of the upper eruptive fissure probably occurred during the late stages of the eruption. The lava flow field continues with two master channels in the middle portion, mostly parallel and oriented NE-SW (Fig. 1a). The NW one is ~ 400 m long and connects the base of the eruptive fissure with the lava apron widening below the village. It has steep levees and is much longer than the SE one which is at most 120 m long and barely visible in the middle-upper portion of the lava flow field. These two channels apparently connect to the lava tubes at the flow front along the shoreline (Calvari et al. 2023). This recent lava flow field is mostly covered by the settlements of Stromboli village except near the beach (Fig. 1a). The erupted lava flowed towards the coast along an old drainage line, forming a lava delta ~ 20 m

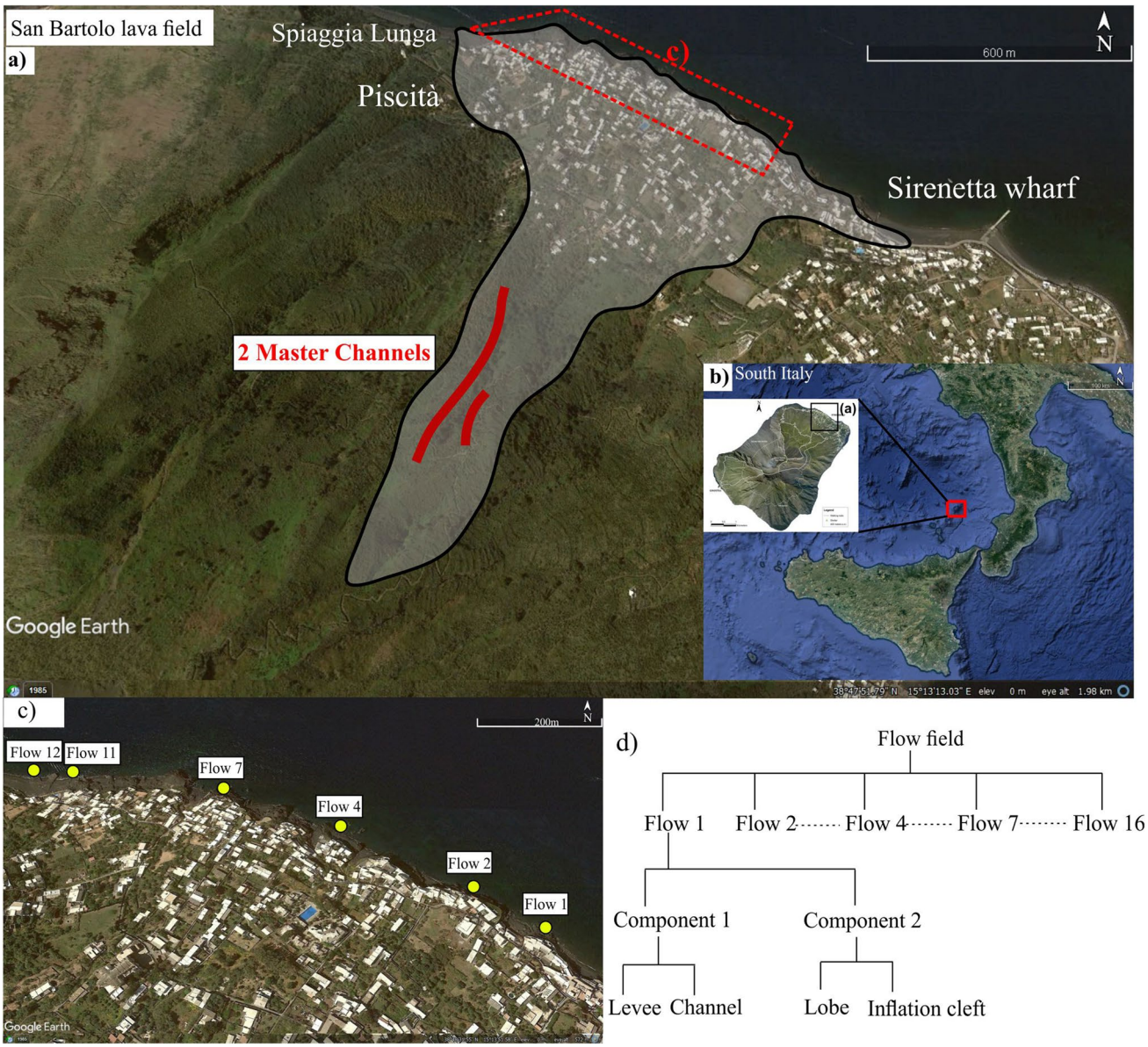

Fig. 1 **a** Google Earth image of the San Bartolo lava flow field of Stromboli volcano (modified after Calvari et al. 2023). **b** The bottom right inset shows the location of Stromboli volcano in south Italy. **c** Google Earth image showing different flows with the yellow dots highlighting the studied flows. **d** Simplified flowchart of the terminologies used in this study

thick and ~ 1 km wide (Francalanci et al. 2013; Calvari et al. 2011, 2023). The lava delta is bounded by the Sirenetta wharf to the east and Piscità to the west (Fig. 1; Calvari et al. 2023). In the SB lava flow field, the well-preserved lava deposition along the coast permitted us to distinguish different morphological features formed by the interaction between lava and sea-water.

The notable difference in the eruptive style during the emplacement of the SB lava field from that of recent eruptions can be seen from the significant changes in the geometry of the magma plumbing system and the change in the composition of the erupted materials (Francalanci et al. 1989; Rosi et al. 2000; Laiolo and Cigolini 2006). The SB lava belongs to Stromboli's high-K calc-alkaline (HKCA) series (Peccerillo and Taylor 1976) and contains abundant phenocrysts of clinopyroxene, olivine and plagioclase, as well as mafic and ultramafic cumulate xenoliths (Laiolo and Cigolini 2006; Calvari et al. 2011; Francalanci et al. 2014).

The SB flow field splits into 16 ocean entry sites of mostly pāhoehoe lava flow lobes (Calvari et al. 2023) here termed 'Flow' (Fig. 1c). Each flow can be divided into different portions, based on characteristic components as illustrated on Fig. 1d.

Methodology

Field survey

Initially, we conducted a thorough survey along the coast of the SB flow field to study the ocean entry of lava and the associated formation of different components. For each of the component, we described and quantified, where possible, its geometry (thickness, width, length, slope and orientation), lithology (colour, degree of alteration and nature of minerals), texture (content, size, number, shape and distribution of vesicle, crystal and void), structures (uniform or brecciated, massive or bedded/layered, with shearing, column, scratch, cooling/quenching structures) and the presence of entrained materials such as enclaves, anthropic material and clinkers. We also carried out a boat survey close to the coast to sample the rocks that were inaccessible from land and to get a broad perspective on lava entrainment into the sea.

Sampling and magnetic measurements

Following the survey, five well exposed and preserved outcrops (Flows 1, 2, 4, 7 and 12; Fig. 1c) were selected for sampling along the coast. We collected a total of 17 oriented hand-samples and 56 oriented drilled cores, in accordance with the standard practice for magnetic measurements (Tarling and Hrouda 1993). The samples drilled near the beach were returned and glued after the measurements. From the collected samples, we drilled out 273 standard cylindrical specimens of 2.5 cm diameter and 2.1 cm length and 11 mini cores of 1 cm diameter and 2 cm in length.

All magnetic analyses were conducted at the Alpine Laboratory of Paleomagnetism (Italy). Initially, the AMS was studied for all specimens to infer the flow fabrics and emplacement process of the lava flow system. AMS provides the magnetic fabric of the rock which is related to the orientation and spatial distribution of all the magnetic minerals in a rock (Cañón-Tapia 2004). The magnetic susceptibility and its anisotropy were measured using the KLY-3 Kappabridge from AGICO. The accuracy of the obtained measurements was assessed using a *F*-test of anisotropy, where data with F values < 5 were eliminated from further interpretation (Hext 1963). We determined the mass magnetic susceptibility (χ_m as standard expressed as $\times 10^{-3}$ m^3 kg^{-1}) to compare the different flows as we have both standard (diameter = 25 mm, height = 22 mm) and mini (diameter = 10 mm, height = 20 mm) cores. The AMS results are represented as an ellipsoid with three mutually perpendicular susceptibility axes: K_1, maximum susceptibility axes; K_2, intermediate susceptibility axes; and K_3, minimum susceptibility axes, where the mean susceptibility is given as $K_m = (K_1 + K_2 + K_3)/3$. K_1 defines the magnetic lineation, and K_3 represents the pole of the magnetic foliation plane which contains the K_1 and K_2 axes. The AMS ellipsoid is defined by scalar parameters including mean magnetic susceptibility (K_m), shape parameter (T) and corrected degree of anisotropy (Pj), which are listed in Table S1 of the Supplementary Material. The distribution of Pj with respect to T provides the shape of the rock fabric. The value of T can vary between −1 and + 1, where $0 > T \geq 1$ is an oblate ellipsoid and $-1 < T < 0$ is a prolate ellipsoid. In general, the oblate ellipsoids result in the distribution of K_1 and K_2 axes along a grid that forms a foliation plane, and the prolate ellipsoid results in clustering of K_1 axes without a defined foliation plane.

To cancel out the aberrations caused by the local occurrence of fan-like distribution of the AMS fabrics at site/sample level, we computed the arithmetic mean of T value to interpret the shape of AMS ellipsoid.

In this study, we use a consistent approach to infer flow direction based on the magnetic fabric type of the AMS ellipsoid (Delcamp et al. 2015; Callot and Guichet 2003). In case of oblate ellipsoids, the imbrication of the foliation plane is used to infer the flow direction, whereas, for those with a prolate ellipsoid, we consider the orientation of the magnetic lineation.

The natural remanent magnetisation (NRM) of all the specimens was measured using the AGICO-JR6 spinner magnetometer. Four pilot samples were demagnetised from each flow unit, two using alternating field (AF) and two by thermal demagnetisation, to select the most appropriate demagnetisation method. Stepwise demagnetisation of the AF was carried out with a field varying from 5 to 120 mT and a thermal demagnetisation with a temperature from 20 °C up to a peak of 600 °C. A total of 61 specimens were demagnetised from five different flow units to isolate the characteristic remanent magnetisation (ChRM). The obtained data were analysed using the software Remasoft 3.0 (Chadima 2006). The remanent magnetisation components were identified using principal component analysis (Kirschvink 1980), and mean directions were assessed with Fisher (1953) statistics.

Analysis of porosity and connectivity

We measured/derived the density/porosity and connectivity of 51 specimens, two specimens per sample, to comprehend the effect of lava-water interaction on the content in vesicles and their connectivity. The envelope volume of the sample, which is the volume of the solid and any pore space or voids within it, was measured using the Geopyc 1360 Envelope Density Analyzer. The skeletal volume, which is the volume

of the solid without the connected vesicles, was measured with a helium displacement AccuPyc II 1350. Both the instruments are housed at Laboratoire Magmas et Volcans (LMV), France, and the measurements were performed following the standard procedures of Thivet et al. (2020). The dense rock equivalent (DRE) of a powdered sample was measured using the Accupyc 1340 Helium Pycnometer. The average DRE of 2920 kg/m^3 from the five measurements was used to calculate vesicularity following Houghton and Wilson (1989), while the connectivity was derived following Colombier et al. (2017).

Clast count method

We conducted a clast count within the pebble-to-cobble range (2–256 mm) at selected sites to infer the character of the eroded offshore segment of the lava flow field and its component flow units. Clast count was performed at four coastal beaches, two at the flow field left lateral margins (Flows 12 and 7) and two at the centres (Flows 1 and 4) (Fig. 1c). At each site, we meticulously counted between 160 and 220 clast selected as representative (making an error around 10% if they represent at least 70% of the total population, following the graph of van der Plas and Tobi 1965) and classified according to phenocryst type and vesicularity. We also extended the clast count to the seafloor for a distance of about 30 m from the shore through a dive survey at Flow 7. Due to the shallow water, this could be achieved with simply mask and snorkel. As with the coastal clast count, seafloor clasts were classified in terms of size, shape, colour and vesicle content. Spatial distribution was set up by swimming out from fixed points along the beach, with a tape measure tied to the diver.

Results

Description of components and magnetic fabric

We first define and describe the five main components of the lava flow system, before mapping their distribution along the zone of ocean entry for the SB lava flow field. We distinguished five main components, which are (1) 'A'ā channel-levee; (2) littoral; (3) ramp; (4) lava tube; and (5) inflated pāhoehoe.

Channel-levee

Channels and associated levees can be observed along the coast. The two master channels are well exposed at Flows 2 and 7 (Fig. 1c) and are NW orientated.

a) Channel at Flow 2

At Flow 2, the contact between the dense, massive, vesicle-free lava of the channel and the left bank levee can be observed (Fig. 2a). The 'a'ā dense channel lava outcrop has a thickness of 14 m and is overlain by a 4-m-thick layer of clinker and ramps. The levee has been preferentially eroded by wave action to form a cave of 8 m in height, and within which, at-least three overflow levees (up to 2 m thick) can be found, with the cave roof being characterised by sheared lava (Fig. 2b). The cave is overlain by 4 m of 'a'ā flow which runs into two overflow units (up to 2 m thick) that mantle the outer flank of the levee.

We collected three hand-samples from Flow 2, one from the dense, massive lava of the master channel (L2A-S3) and two from the overflow levee of the eroded cave (L2A-S1 and L2A-S2). The mass susceptibility ranges from 1.63 to 8.63 (10^{-3} m^3 kg^{-1}), with an average value of 4.25 ± 3.340 (10^{-3} m^3 kg^{-1}) (Table S1). More than 90% of the studied specimens show oblate ellipsoid and are characterised by a low corrected degree of anisotropy (Pj = 1.003–1.011) (Table S1), which is normal for a lava flow (Cañón-Tapia and Pinkerton 2000). Stereographic projection of the susceptibility axis displays a good clustering for sample L2A-S2, whereas the rest of the two (L2A-S1 and L2A-S3) disperse axes along the K_1-K_2 plane (Fig. 2a). The samples L2A-S1 and L2A-S3 exhibit a similar distribution of susceptibility tensor with a vertical foliation plane striking WNW-ESE and the K_3 axes forming a cluster along the N-S direction (Fig. 2a). The stereographic projection of L2A-S2 shows a sub-vertical to inclined foliation plane with the K_3 axes striking NE-SW.

b) 'A'ā channel at Flow 7

The right bank rubble levee of the 'a'ā master channel for Flow 7 is exposed at the Grotta di Eolo, another cave system created by erosion of the breccia. The rubble levee is 9 m high and 30 m wide and is capped by a 3.5-m-thick overflow levee of massive, vesicle-free lava with shear partings and elongated entrainment bands (length from 0.5 to 1.5 m) (Fig. 3a). Towards the levee base, capping the cave is a unit of identical character to the overflow unit (Fig. 3), and this may be an intrusion of dense lava into the rubble levee. The rubble is organised into sheared bands of aligned breccia (up to 5 to 10 cm in thickness), with the sense of shear being up and over the levee to the SSE (Fig. 3). All directional markers are consistent with the same SSE deformation, overflow, and intrusion direction, as detailed on Fig. 3b.

We drilled cores from the massive lava (L7B) and the sheared plates on the cave roof (L7C). The mass magnetic susceptibility shows a mean value of 6.21 ± 0.35 (× 10^{-3} m^3 kg^{-1}) (Table S1). The mean corrected degree of anisotropy (Pj = 1.016) is the highest among the whole sampled sites. As with the 'a'ā channel described above

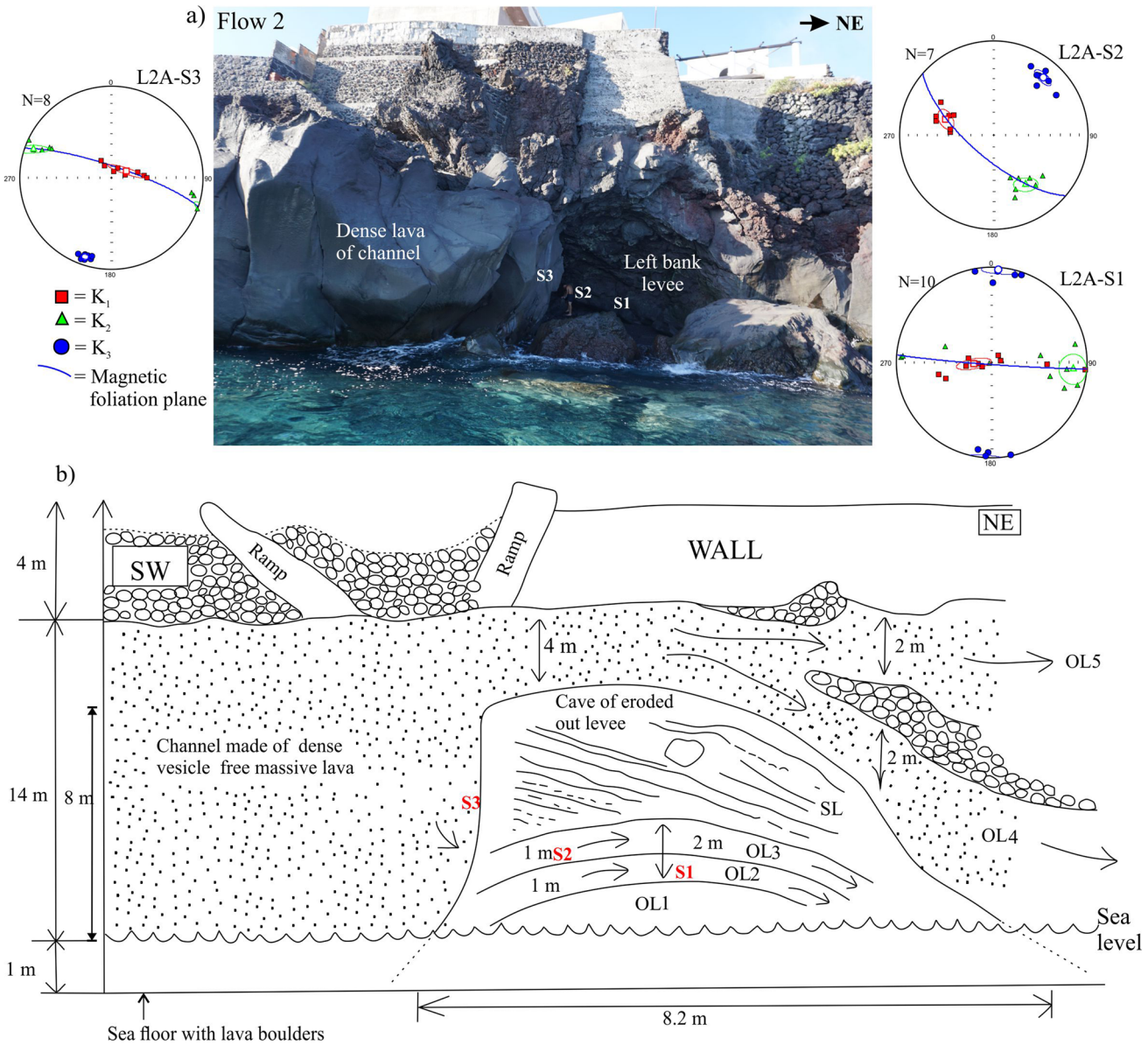

Fig. 2 **a** Field photo of 'a'ā master channel at Flow 2 showing the location of sampling and AMS result. Lower hemisphere equal-area projection shows magnetic lineation (K_1) and foliation (K_1-K_2). **b** Diagram of 'a'ā channel and associated levees with measured field parameters. OL, overflow levee; SL, sheared lava. The red labels correspond to the sampling locations

for Flow 2, the 'a'ā channel observed at Flow 7 also shows mainly oblate ellipsoid. In the stereographic projection, L7B is characterised by moderate to steeply dipping foliation plane striking NNW-SSE (Fig. 3b). In the case of L7C, the foliation plane is gently dipping and strikes along NNE-SSW direction (Fig. 3b).

Littoral component

The littoral component is extremely chaotic and is well-exposed just 20 m to the east (along shore) of the inflated pāhoehoe Flow 11 (Fig. 1c). It is oriented S-N, has a total thickness of 3 m and comprises six 'a'ā flow units (Fig. 4):

A. Inland, the lower portion is 1.6 m thick and contains entrained pockets of 'a'ā clinker up to a meter across, where vesicles (up to 1 cm in diameter) are deformed around the pockets (Fig. 4). The base of unit A is buried by beach cover, but a crust of 'a'ā clinker can be found.
B. Unit A is overlain by a vesicular 'a'ā unit of 40 cm thickness with pyroxene phenocrysts up to 4 mm across (Fig. 4). The contact with unit A is marked by a shear zone.

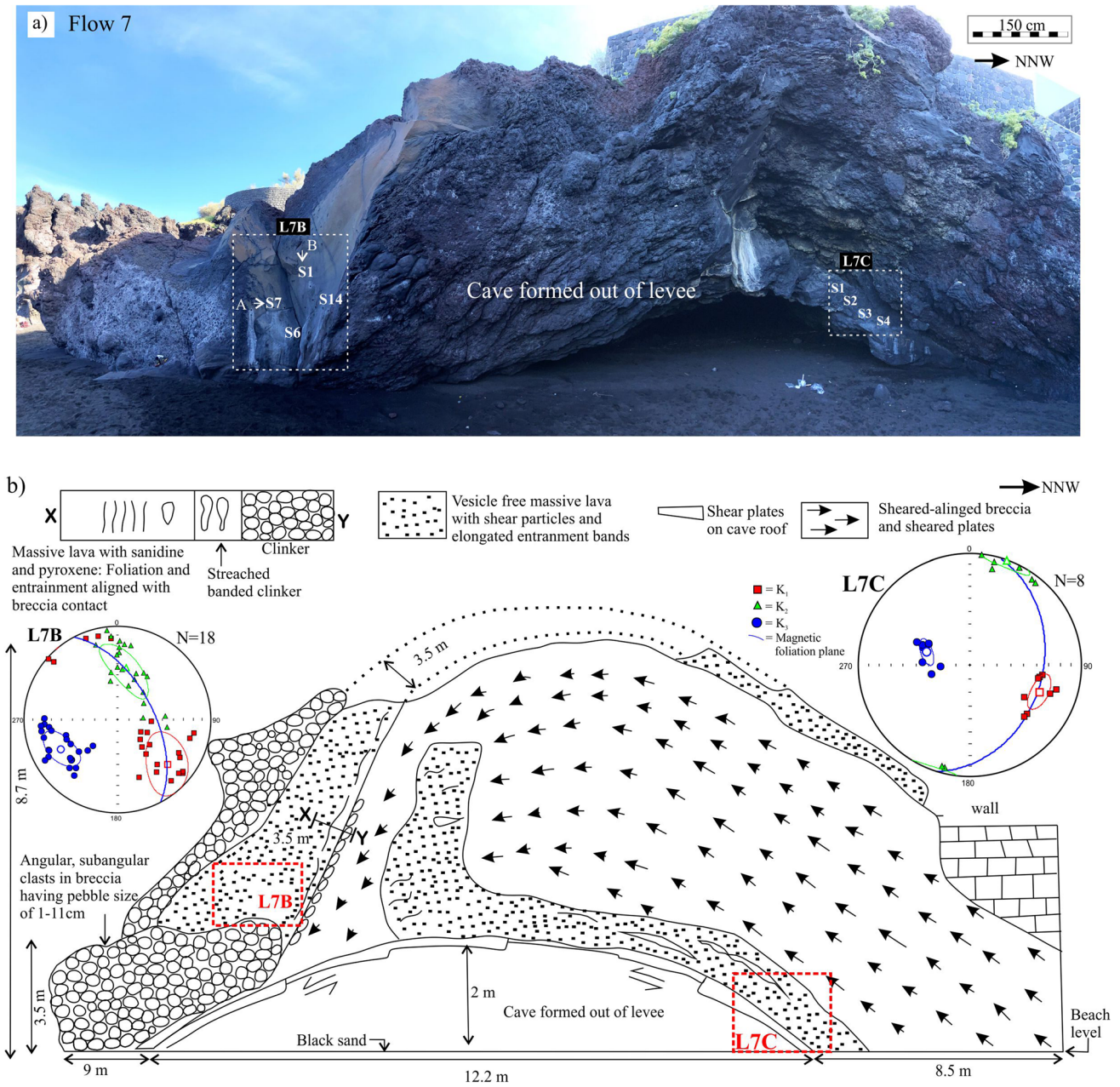

Fig. 3 **a** Field photo of channel at Flow 7 above the Grotta di Eolo, showing two sampling location (site L7B and L7C) marked with dotted rectangular lined. **b** Sketch of master channel with AMS results. The top flow is partially eroded above the cave, as evidenced by the dotted lines, for a thickness of about 3.5 m. The red labels correspond to the sampling locations; the arrows indicate flow direction of emplacement

C. Seawards, units A and B become broken into tilted blocks of 'a'ā (Fig. 4). Blocks have the same mineralogy as units A and B, and their thickness (1.8 m) is approximately the same thickness as units A and B.
D. Between units A–B and C is a zone of rubble, mixed with slabs of lava having thickness if 1 m and pockets, up to 35 cm across, of 'a'ā clinker.
E. All units are overlain by a coherent unit of vesicular 'a'ā that drapes over the underlying units. The unit is 80 cm thick and contains 1–5 mm diameter vesicles and phenocrysts of olivine up to 4 mm. This unit is underlain by 30–60-cm-thick layer of tilted plates (E'). This appears to have been formed by break-up of the basal shear zone of unit E (Fig. 4a).

Because these units broke into blocks (up to 1.3 m), which were then tilted and rotated to varying degrees (Fig. 4), we did not sample any littoral component for AMS analysis.

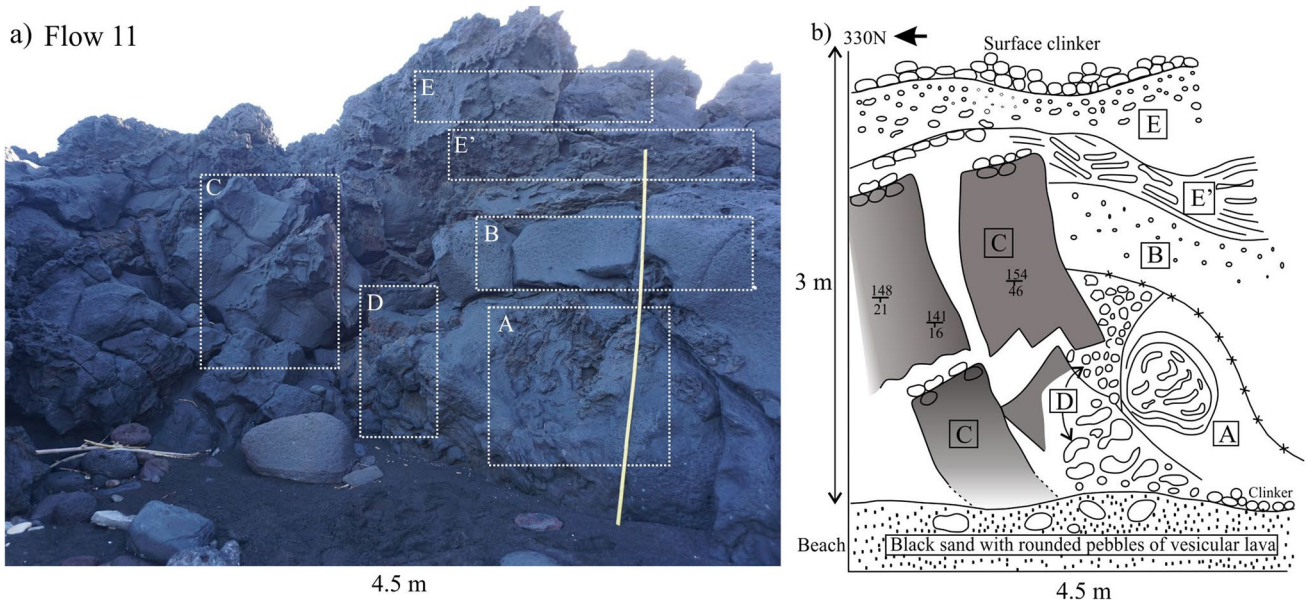

Fig. 4 **a** Field photo of the extremely chaotic littoral component at Flow 11. The ruler is 2 m high. **b** Sketch of littoral component with five different units. Attitude of tilted blocks of vesicular lava measured from field is marked in the figure. A, lower part which contains balls of 'a'ā clinker; B, less vesicular 'a'ā unit, which shows a sheared contact with A; C, tilted blocks of vesicular 'a'ā lava; D, pockets and basal layer of 'a'ā clinker; E, overlying vesicular 'a'ā draped over underlying units; A', tilted plate of shear zone of unit A

However, strikes and dips of blocks were taken and are given in Fig. 4. The highly variable and mixed textural character of this component also meant that we did not sample this unit for vesicularity quantification.

Ramp

Ramps can be observed along the entire coast from Spiaggia Lunga to the Sirenetta wharf (Fig. 1a), with the 'a'ā ramp zone extending for 10's of meters inland where it underlies the village (Fig. 1c).

a) Ramp at Flow 7

Ramping is characterised by upward thrusted slabs of 'a'ā that became stacked in sequence behind the flow front, up to 10 m (Fig. 5a). Ramps run down into the massive interior, developing an orientation from sub-vertical to vertical towards the flow surface. Entrained clinker pockets (160 cm) and detached bands of deformed clinker can be found between ramps (Fig. 5b). Below the ramp structures, behind the concrete wharf, lava is massive and dense with horizontal foliation and tension gashes. The best overview of ramping is at Flow 7 where exposure runs 70 m inland. Here, the sense of shear marked by tension gashes of 20–30 mm in length is 4° N, which is the same as the orientation of the ramping.

Samples were collected along two parallel vertical transects to study the variation in flow fabrics along the ramp length. The mean mass susceptibility is 6.84 ± 3.16 ($\times 10^{-3}$ m^3 kg^{-1}). The shape of the AMS ellipsoid includes both oblate and prolate fabrics ($-0.430 < T < 0.590$), with a prevalence of oblate fabrics. Similar to the other site, this site also has a low mean corrected degree of anisotropy (see Pj values in Table S1).

The resulting magnetic fabrics show a wider scattering, with K_1 axes forming three different clusters, where the clusters show no relation to the spatial distribution of the specimen. This allowed us to classify them into three sub-fabrics: (a) prolate fabrics with gently dipping magnetic foliation and NW-striking magnetic lineation (Fig. 5c); (b) oblate fabrics with gently dipping magnetic lineation and steeply dipping NE-SW striking magnetic foliation (Fig. 5d); and (c) oblate fabrics with NE-striking magnetic lineation and NE-SW striking magnetic foliation plane (Fig. 5e). The third sub-fabric is characterised by the formation of fan-like distribution of AMS axes that masks the oblate fabrics of single specimens by a bulk prolate ellipsoid at site level.

b) Ramp at Flow 1

The detail of an individual ramp is particularly well exposed at Flow 1 (Figs. 1c and 6). Here, we focus on an 'a'ā lava flow unit 7.3 m in height. The whole structure can be grouped into three zones, from bottom to top: (1) a vesicular lava, (2) a massive dense lava, and (3) a ramp. At the base is a 2-m-thick layer of vesicular lava. Vesicle size decreases with depth from 5 to 15 mm at the top to 1–2 mm

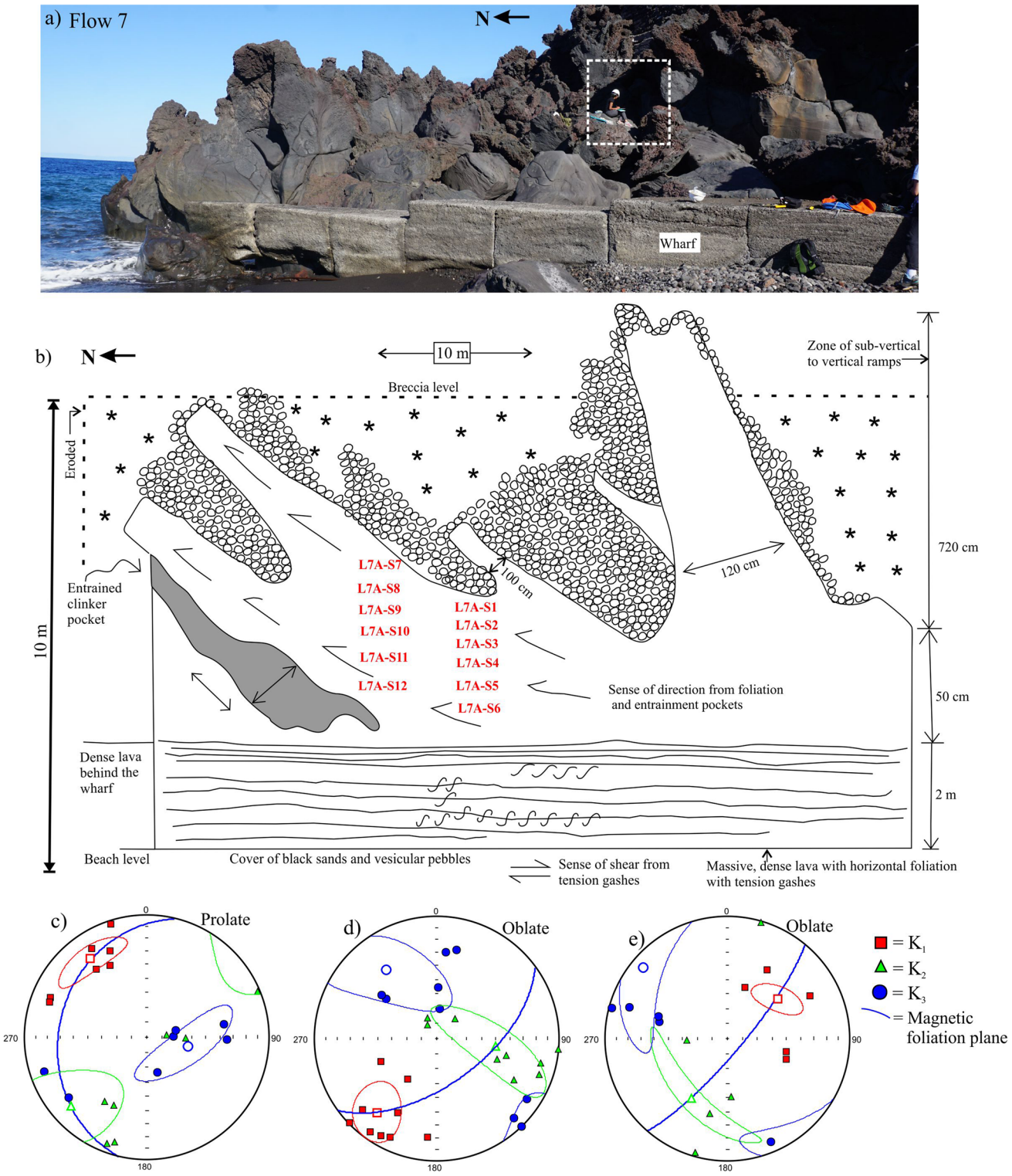

Fig. 5 **a** Photo of the ramp observed at Flow 7 where the white dotted box highlights the sampling location shown in **b**, with samples positions indicated by the red labels. **b** Sketch of ramps with the sense of flow direction measured in the field. The red labels correspond to the sampling locations. **c**, **d**, **e** Principal susceptibility axes distribution on lower hemisphere equal-area projections

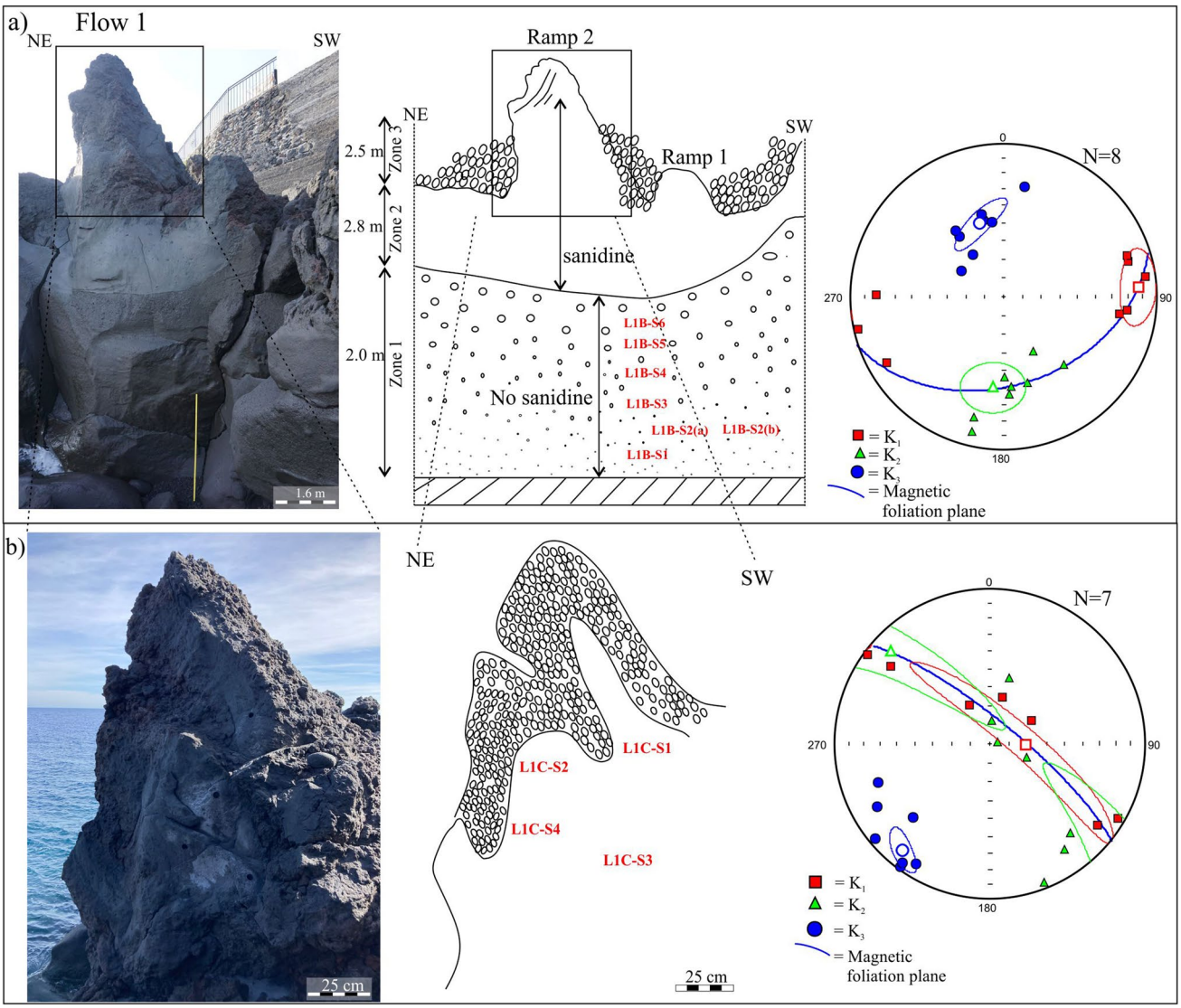

Fig. 6 **a** Photo and sketch of the lava unit with ramping, massive dense lava, and vesicular lava, Flow 1. For sampling, we considered the lower two zones together and the upper ramp zone separately. **b** Photo showing a detail of the Flow 1 ramp zone with sampling sites. The red labels correspond to the sampling locations and the equal-area projection shows the AMS fabric

at the bottom (Fig. 6a). Above, there is a 2.8-m-thick layer of massive dense lava with entrained clinkers (Fig. 6a). These clinkers are aligned and orientated 44° NE. The ramp zone comprises the uppermost 2.5 m and has two sub-vertical ramps of 'a'ā (Fig. 6b). The lava flow is sheared and characterised by deformed vesicles, ~20 mm in length, with entrained 'a'ā clasts up to 10 cm in diameter. Structures and shearing are aligned 44° NE. While the contact between zones 1 and 2 is gradational, that between zones 2 and 3 is abrupt (Fig. 6a).

Cores were drilled from the bottom vesicular lava (zone 3) and the top ramping structure (zone 1) to characterise the variation in the flow fabrics along the vertical transect. The bulk χ_m shows no significant variation among the two zones (Table S1). The mean degree of anisotropy is similar to the rest of the flow units (Pj = 1.008), and the shape of the AMS ellipsoid is oblate. In the ramp zone, the magnetic foliation plane is steeply dipping and strikes NW-SE (Fig. 6b), whereas in the bottom vesicular lava, the three susceptibility axes are well clustered with an inclined foliation plane striking along ENE-WSW (Fig. 6a).

c) Ramp at Flow 4

At Flow 4 (Fig. 1c), we find a ramp cut in three dimensions, along and across the axis of ramping (Fig. 7). As at all flows, ramps are stacked parallel to the shoreline with a long axis oriented 345° N. Five 'a'ā ramps can be identified,

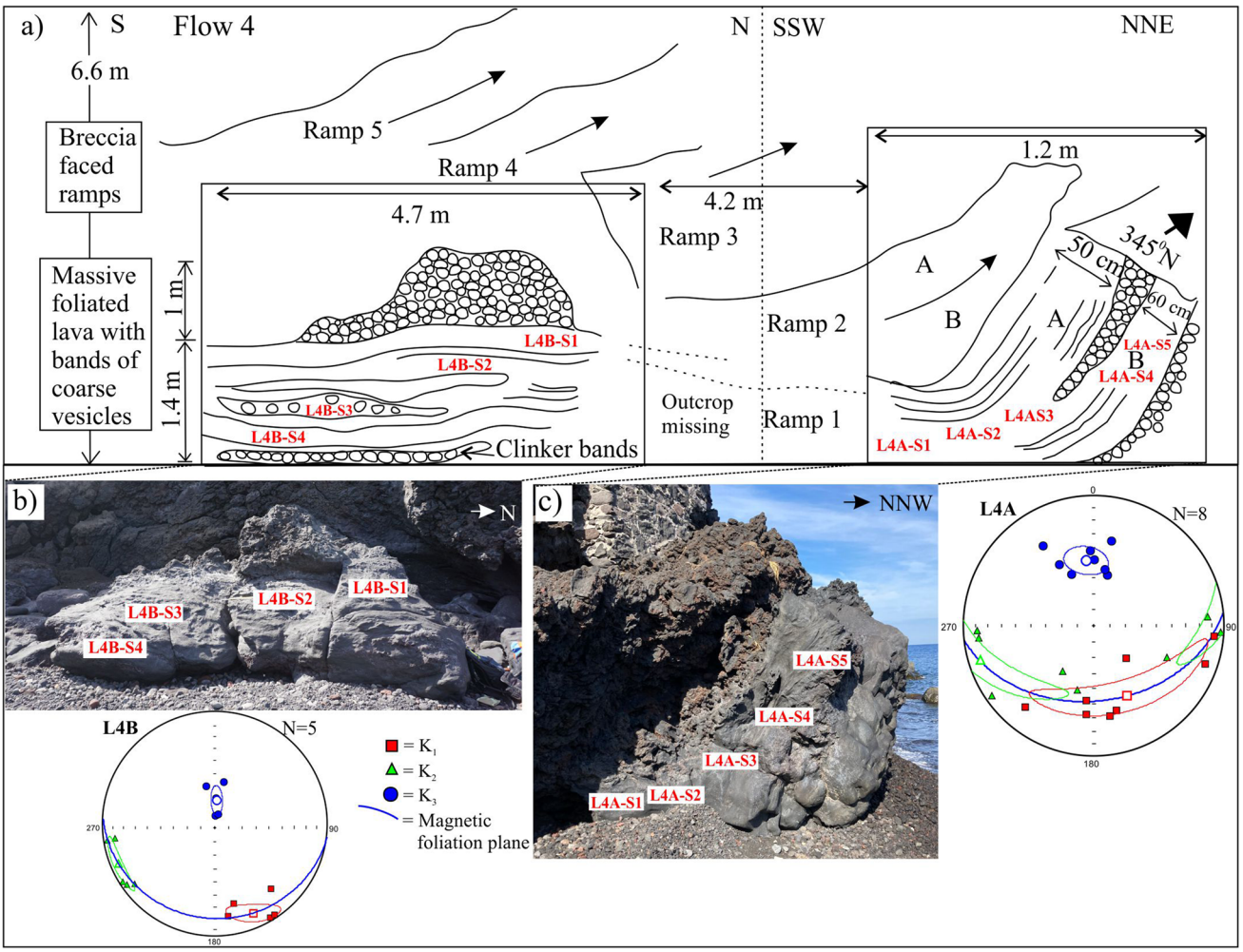

Fig. 7 Ramp cut in three dimensions observed at Flow 4. **a** Sketch of ramping showing the parallelly stacked ramps with foliation direction indicated by sheared lava. **b** and **c** show the southern and northern part of the ramp with the location of sampled cores, respectively. Stereographic projection obtained from AMS study shows the distribution of the three main susceptibility axes

stacked in sequence along the flow direction (55° N; Fig. 7a). Ramp 1 is 1.4 m thick and is characterised by massive, foliated lava with bands of coarse (1–4 mm) vesicles. While the southern part of the outcrop cuts the ramp in the crossflow direction (Fig. 7b), the northern part cuts it in the downflow direction (Fig. 7c). The downflow section shows two massive parts to the ramp separated by an entrained clinker band, which is cut in the crossflow direction in the southern part of the outcrop (Fig. 7). Subsequent ramps also have almost similar characteristic features of thick massive core and clinker top with thickness varying between 1.0 and 1.4 m.

Here, we drilled the cores from the crossflow (L4B) and the downflow section (L4A) of ramp 1 (Fig. 7a). The χ_m is consistent with the other components observed ($\chi_m = 5.95 \pm 2.55 \times 10^{-3}$ m^3 kg^{-1}), and the corrected degree of anisotropy is low (Pj = 1.008). On the northern half of the ramp, the magnetic foliation is moderately dipping and strikes E-W (Fig. 7c), whereas, on the southern half, the foliation plane dips gently along E-W (Fig. 7b). In both cases, the pole of the foliation plane is parallel to the strike of the ramp, and the K_1 and K_2 axes distribute along a girdle making a well-defined foliation plane.

Lava tube

From our field investigation, we identified the presence of tubes across the barrier of the sea surface to feed a seaward bench of pāhoehoe around most 'a'ā flow units. The best preserved example was found at Flow 1 (Fig. 1c). Here, we found two tubes, extending both NE from a wide vent at the base of a 4 m high 'a'ā flow front. The best developed tube is in the eastern branch, which can be followed for a distance of 15 m. It is 1.6 m high, and 3.6 m wide, trends 34° N before turning 58° N (Fig. 8a) and has a slope to the NE of 11–12°. The tube walls are characterised by at least five accreted layers with thicknesses of 9–16 cm (Fig. 8b),

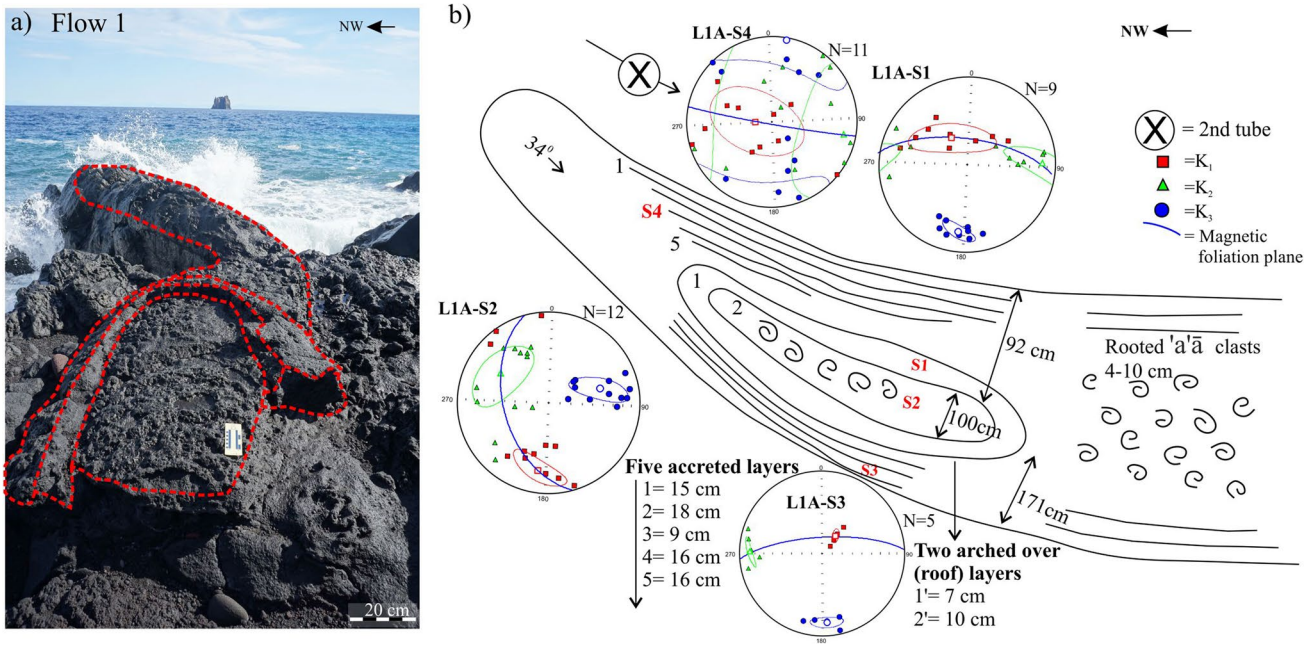

Fig. 8 **a** Photo of the tube observed at Flow 1 exit (2nd tube is not visible in the photo). **b** Sketch of tube along with the sampled location, view from above. The stereographic projection shows the orientation of three susceptibility axes and foliation planes. Accretionary layers (1 to 5) and arched over roof layers (1' and 2') are highlighted in the sketch and numbered from outer to inner layer

characterised by accreted clinkers elongated in the direction of the tube orientation. The roof comprises two arched-over layers with a thickness of 7 and 10 cm. The exposed central stream (Fig. 8) is 0.9 m wide and has embryonic 'a'ā clasts rooted to the interior lava. The second tube shows the same pattern, but is less well exposed, being eroded by wave action. However, it shows the same form with the tube cavity that has a height of 1.4 m and three accreted layers.

We collected four hand-samples, one from the central stream (L1A-S2) and three from the accretionary layers (L1A-S1, L1A-S3 and L1A-S4) for magnetic fabric study. Figure 8 and Table S1 show the distribution of the susceptibility axes for each sampling site and the final AMS results, respectively. The bulk χ_m shows an average value of 2.91 ± 0.36 ($\times 10^{-3} m^3 kg^{-1}$). The Pj value ranges from 1.001 to 1.017, with an average value of 1.006 (Table S1). Samples collected from the opposite sides of the accretionary layer, NE and SW, show neutral to oblate fabrics, while the central stream shows a mixed fabric. Looking at the distribution of principal susceptibility axes, the magnetic fabrics show well grouped axes, with the exception of L1A-S4 (Fig. 8b). Samples from the accretionary layers show sub-vertical foliation planes with an E-W orientation, while the central stream shows an inclined foliation plane striking NNW-SSE (Fig. 8).

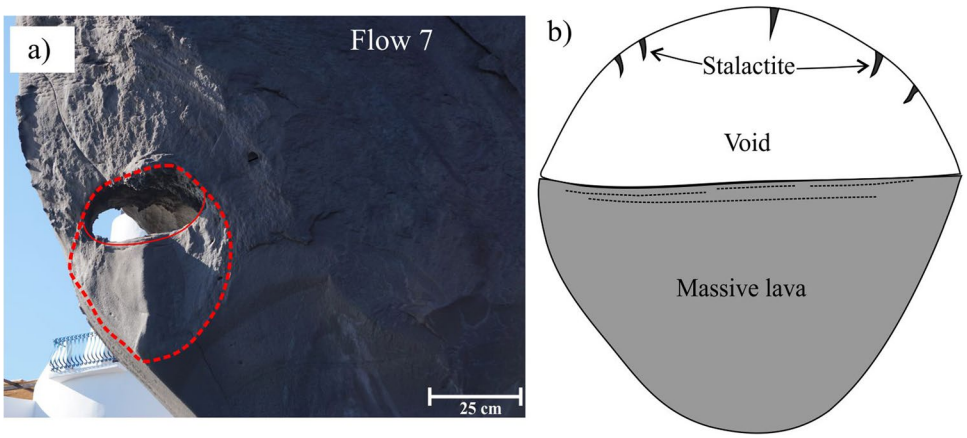

Fig. 9 **a** Field photo of tube observed at the cliff of Flow 7. The boundary of the tube is marked with red dotted lines. **b** Section of the observed tube showing the stalactite at the roof of the void space and massive lava with upper foliations

A second tube can be found exposed high in the cliff at Flow 7 (Fig. 1c). This tube is partially drained and is 50 cm wide and includes 25 cm of empty space (Fig. 9a). The roof displays stalactites and is above a pāhoehoe flow surface (Fig. 9b). Undrained lava is vesicular (with vesicles up to 5 mm in diameter) and surrounded by dense lava of the flow front through which the tube cuts.

Inflated pāhoehoe

Inflated pāhoehoe can be found all along the coast, especially at the NW and NE margins of the SB lava flow field (Fig. 1c). The best exposed example is Flow 12 at the NW edge of the lava flow field, where two inflated pāhoehoe flow units can be traced for a distance of 24 and 33 m towards NW and north, respectively, with a uniform width of 11 m (Fig. 10a). The interior is made of dense lava with sheared vesicles (up to 50 mm), and the sense of shear is in the direction 196° N with a slope of 12° downwards to the north (Fig. 10b). The thickness of the interior increases towards the sea from 1.4 mto 3.2 m. At the same time, a vesicular surface layer can be identified down the entire length of the unit that varies in thickness from 1 to 3 cm. The unit can be divided into four pāhoehoe lobes, which vary in length from 1.3 to 11 m, each being separated by an inflation cleft (Fig. 10a–c). In the transverse section, vesicles are oval, small and numerous towards the surface and increase in size from 1 to 5 mm, while decreasing in number towards the lobe centre (Fig. S1a). Vesicles also become more sheared towards the lobe centre, with sense of shear being around a central void (Fig. S1b).

We collected two hand samples near the inflation cleft (L12-S5 and L12-S6), eight hand-samples from the top of the vesicular surface layer and six drilled cores from the lateral side of the dense interior lava (Fig. 10a–b). The χ_m shows a mean value of 2.14 ± 1.49 ($\times 10^{-3}$ m^3 kg^{-1}) (Table S1). The corrected degree of anisotropy Pj is relatively low, ranging between 1.001 and 1.013 (Table S1). The susceptibility ellipsoids are mostly oblate and are independent of the degree of anisotropy. For the degree of anisotropy and the shape parameter, no significant differences are observed with respect to the position of the samples (Table S1).

Samples from the top of the vesicular surface layer show vertical to sub-vertical foliation planes with distinct orientations (Fig. 10a). For example, samples L12-S7 and L12-S10 provide a vertical foliation oriented ENE-WSW, whereas L12-S1 and L12-S2 show a vertical foliation plane along NW-SE (Fig. 10a). Here, the K_1 and K_2 axes distribution makes gridles, defining good foliation planes, except for two locations (L12-S8, L12-S9). Samples from the inflation cleft are well clustered, with an E-W oriented sub-horizontal foliation plane and north dipping magnetic lineation (L12-S5 and L12-S6 in Fig. 10a). Unlike the surface layer, the dense lava of the centre core displays a sub-horizontal foliation plane striking in the NE-SW direction (Fig. 10b).

Palaeomagnetic results

The paleomagnetic findings are presented using orthogonal vector plots (Zijderveld 1967), revealing the demagnetisation characteristics of each specimen (Fig. 11a and b). Both AF and thermal demagnetisations show a stable magnetisation intensity and a well-defined single magnetisation component. The intensity of natural remanent magnetisation of the sampled flows shows a wide range, from 3.17–70.64 Am^{-1} (Table S2). Relatively high NRM intensities (> 30 Am^{-1}) were recorded for tube, inflated pāhoehoe and channel-levee components (Table S2). Most samples are characterised by univectorial orthogonal plots, as expected for recent lava flow (Fig. 11). A few samples show the presence of secondary viscous remanent magnetisation easily removed within the first few steps of demagnetisation.

The characteristic components were estimated by the stepwise demagnetisation, selecting a maximum angular deviation (MAD) threshold of 3°. The ChRM is mostly isolated around 450–540 °C for thermal demagnetisation (Fig. 11b). Instead for AF demagnetisation, more than 90% of the sample was completely demagnetised around 100–120 mT (Fig. 11b). For the rest 10%, complete demagnetisation required higher magnetic field, >120 mT. The mean-site ChRM was calculated with Fisher's statistics. The obtained ChRMs show mostly north declinations and positive inclination, consistently with the geocentric axial dipole (GAD) direction at the geographic coordinates. The mean-unit ChRM direction of SB lava flow is: inclination (I_{mean}) = 59.8°; declination (D_{mean}) = 1.2° with precision parameter (k) = 37 and α_{95} confidence cone = 3.4 (Fig. 11c).

Porosity and connectivity distribution

The distribution of connectivity with respect to porosity of the SB lava is summarised in Fig. 12. All the analysed samples displayed a high value of connectivity, which is typical of the rocks formed by effusive eruption, especially for basaltic lava flows (Colombier et al. 2017). The small dispersion of connectivity, between $0.95 < C < 1.01$ for ramp and channel, make them different from inflated pāhoehoe and tube having $C \approx 1$ (Fig. 12, Table S3). This division is even better for the porosity distribution (Fig. 12). Porosity varies between 0.5 and 15% for ramp and channel and 20–35% for inflated pāhoehoe and channel-levee system (Fig. 12). Furthermore, the distribution of connectivity and porosity shows a negative correlation, with the connectivity value becoming more distributed as the porosity of the rock decreases (Fig. 12).

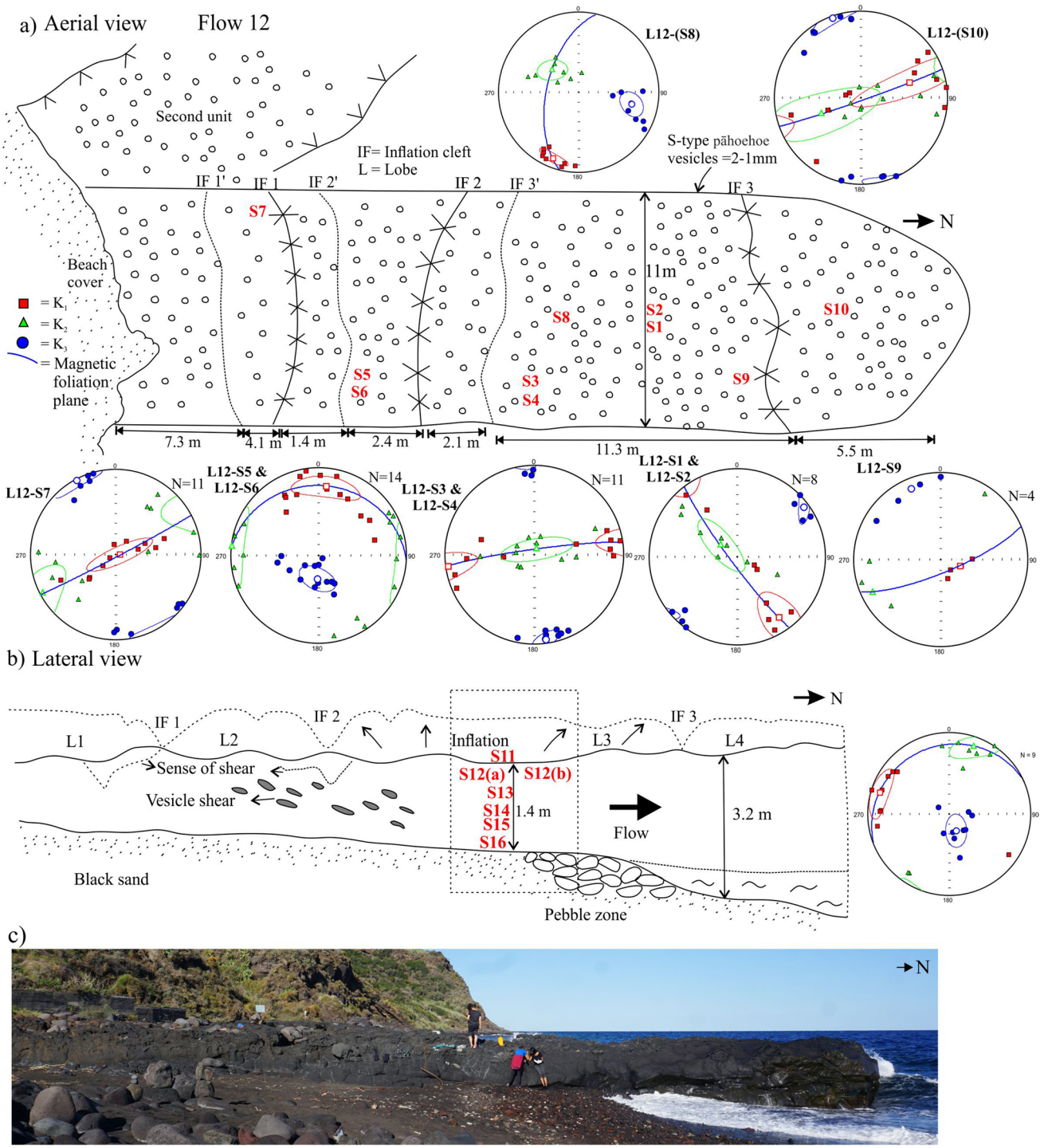

Fig. 10 **a** Aerial view of the inflated pāhoehoe lobes comprising Flow 12, showing the sampled location and the representative stereoplots. **b** Lateral view showing the sampled sites along with the stereographic projection of the results. The thick black arrow shows the flow direction, the small upper arrows the inflation directions measured in the field. **c** Field photo showing the lateral view of the Flow 12 inflated pāhoehoe entering the sea

Clast counts

Texturally, clasts at all sites could be divided into five groups: (1) clinker; (2) oxidised; (3) finely vesicular (Fv, vesicle size ≤ 4 mm); (4) coarsely vesicular (Cv; vesicle size ≥ 5 mm); and (5) dense. In terms of phenocryst content, they could be divided into sanidine-rich and olivine-bearing. Figure 13a shows the spatial distribution of the

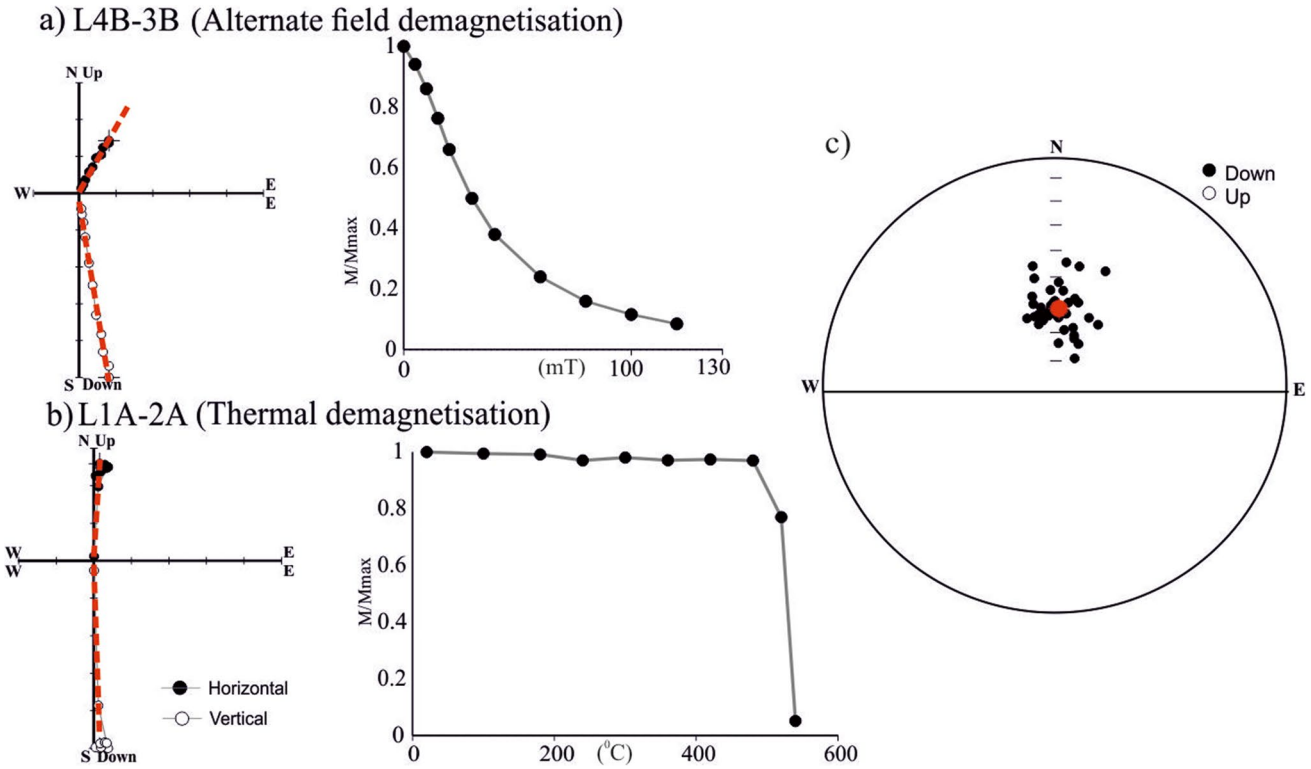

Fig. 11 **a** Alternate field and **b** thermal demagnetisation behaviour of two representative specimens showing stereographic projection, normalised intensity curve (M/M_{max}) and orthogonal projections. **c** Site mean ChRM direction with α_{95} confidence limits

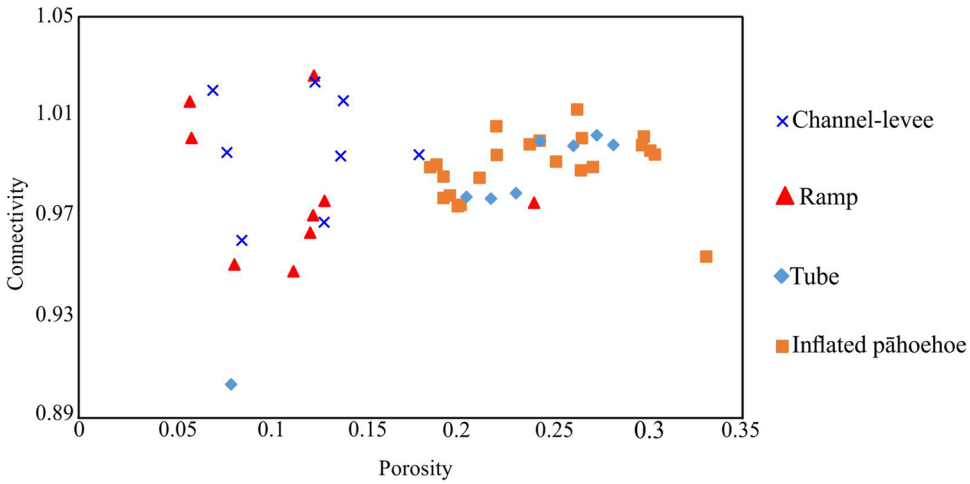

Fig. 12 The covariance of connectivity with porosity for ramp (triangle), tube (diamond), inflated pāhoehoe (square), and channel-levee (cross)

different clast types along the coast. In general, all clast counts are dominated by coarsely and/or finely vesicular lava, with minor amounts of oxidised and dense lava plus clinkers. While the occurrence of coarsely vesicular lava increases as we move along the coast to south-east, the incidence of clinker and finely vesicular lava decreases (Fig. 13a). Also, as we move to north-west, the quantity and size of olivine phenocrysts decreases, and the number of sanidine-bearing clasts increases. At the dive site, offshore of Flow 7, we find a shallow platform with a seaward extension of 30 m (Fig. 13b). Sea floor clasts are dominated by finely vesicular lava, with concentrations of dense lava and clinker aligning with onshore channels and levees. Clast size also increases seawards, and a zone of oxidised lava can be found aligning with an onshore outcrop of the same character (Fig. 13b).

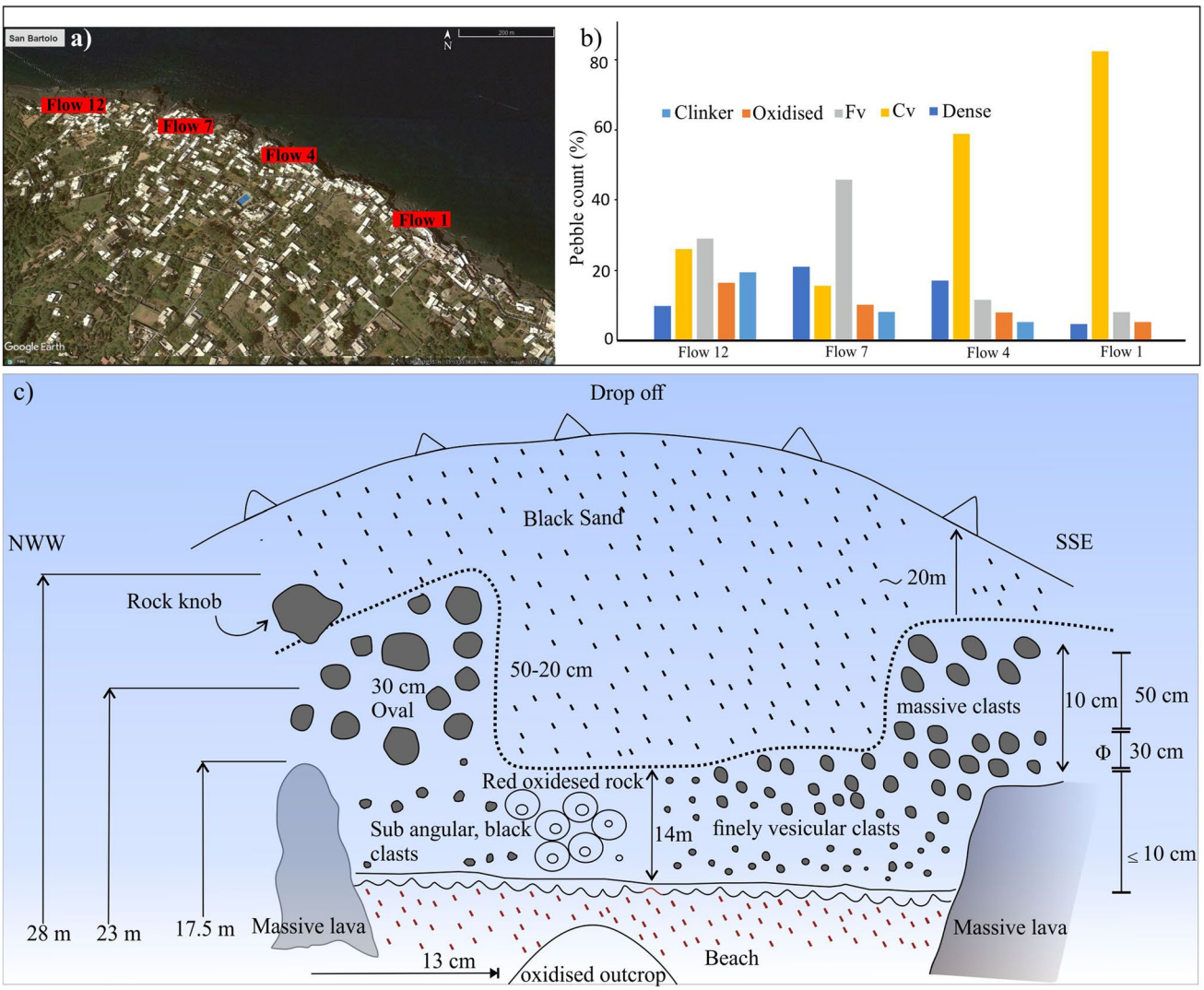

Fig. 13 **a** Google map of the lava flow units highlighting the flows selected for clast counting. **b** Histogram showing the distribution of clasts along the coast. Fv, finely vesicular; Cv, coarsely vesicular. **c** Sketch of an overview of sand and boulder distribution in the shallow region of sea obtained from the dive survey

Discussion

We first describe the magnetic flow fabrics and the emplacement dynamics of each component, before building an interpretative model for the formation of a channel-fed 'a'ā lava flow entry into a water system.

Magnetic flow fabrics and emplacement mechanism of lava

The AMS study aids to characterise the flow fabrics of each component and to evaluate the lava flow dynamics and emplacement sequence. Our results highlight the remarkable agreement between the flow direction derived from AMS measurements and the contextual conditions specific to the local environment. In addition, the mean ChRM direction obtained from our study (I_{mean} = 59.8°; D_{mean} = 1.2°) is consistent with Arrighi et al. (2004) who found I_{mean} = 53.4°, D_{mean} = −4.2°, k = 386 and α_{95} = 1.5 for the same flows. In addition, Speranza et al. (2008) gives I_{mean} = 60.0°, D_{mean} = 359.3°, k = 143 and α_{95} = 1.7. Thus, our data are in agreement with the archaeomagnetic age of ~2–4 ka given in the literature (Arrighi et al. 2004; Speranza et al. 2008).

'A'ā flow channel-levee

The two master channels formed inland along the middle portion of the SB lava flow field probably connected with Flows 2 and 7, to feed the main ocean entry of lava (Fig. 1c). The central lava channel is characterised by the flow along

NE-SW direction (Fig. 14). This lava stream is bounded on both sides by right bank (RB) and left bank (LB) levees, consisting of an overflow, shear and rubble levee (Fig. S2). The initially formed rubble levee is overlayed by the sheared and overflow levee (Hulme 1974; Sparks et al. 1976; Harris and Rowland 2015; Lipman and Banks 1987).

At Flow 2, the upstream flow along the channel to feed the overflow levee is marked by a vertical foliation oriented E-W to NW-SE. The increased flatness of the AMS ellipsoid ($T = 0.600$) is attributable to the significant shear at the channel boundary (Cañón-Tapia and Pinkerton 2000). Disregarding the samples from the overflow levee to avoid the local variations in the flow direction, the samples collected from the massive lava channel show a SSW flow direction. For the second channel at Flow 7, the well-defined foliation plane and strong oblate ellipsoid provide a flow direction towards

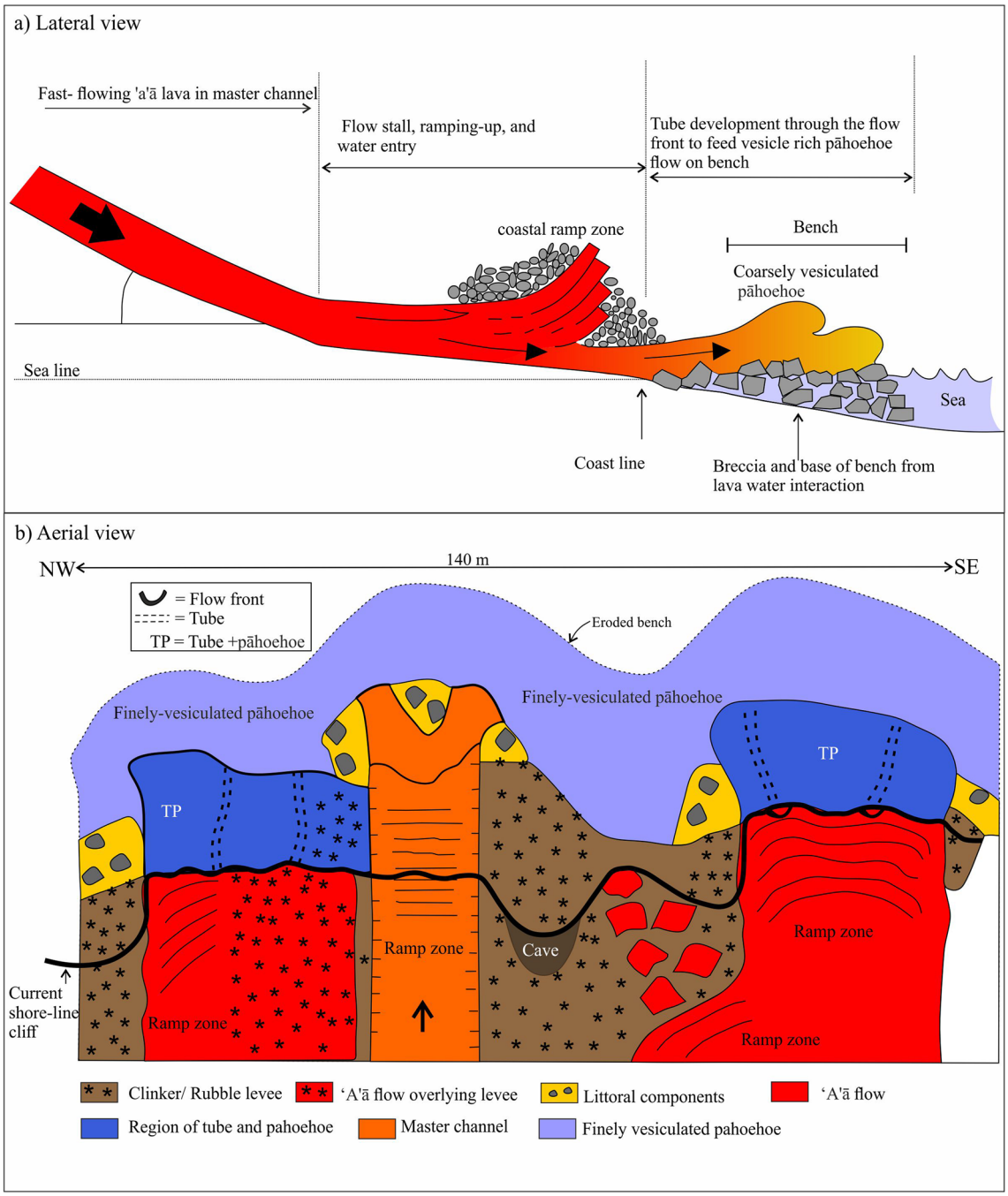

Fig. 14 Schematic illustration showing **a** lateral and **b** aerial views of lava entry into the ocean and the spatial distribution of associated major lava flow components. The central lava channel shows model 2, and the two lateral channels show model 1

WSW (Fig. 3). For both cases, the obtained flow direction is opposite to the regional flow of the SB lava flow field with the foliation plane dipping towards the known flow direction. The resulting flow direction shows the backward flow of lava in the channel as the lava flow slows down at the shoreline due to the development of pāhoehoe benches.

Littoral component

The littoral features formed across the zone of lava-water interaction. The lava-water interaction is a fast and complex process where the explosive intensity mostly depends on the influx of lava into the sea water (Mattox and Mangan 1997; Bosman et al. 2014). The outcrops along the coast observed at SB were formed by the two lava fluxes (Flow 2 and Flow 7), the first of which underwent flow wide break-up and mixing, while the second flowed over the basal unit while remaining intact. The chaotic and reworked character of the littoral component precludes us from studying and interpreting magnetic fabrics.

Ramps

Ramping occurs when the lava flow front stalls, and the subsequent lava flow moves upward with the shearing of internal layers due to thrust from the stalled lava flow front (Macdonald 1972). Here, ramps were formed as the lava backed up in channels behind the ocean entry. The lava ramps up as fast-flowing lava from the main channel encountering the break in slope and later stalls (Fig. 14). The vertical to inclined foliation planes observed in all three cases (Flow 1, Flow 2 and Flow 7) are due to the vertical upward sliding of the lava due to ramping.

In the case of the ramp observed at Flow 1, the distribution of the susceptibility axes shows different patterns for the upper and lower part of the ramp. The NNW flow direction obtained for the lower part is inconsistent with the known strike direction of the SB flow field. This is probably due to post-emplacement modification by the continuous inflow of lava below the ramp structure to feed the pāhoehoe bench. In fact, the sample collected from the top of the ramp, i.e. away from the subsequent flows, gave a more reliable result with a vertical foliation plane and NE-SW flow direction (Fig. 6b). Therefore, we avoided considering the lower part of the ramp for flow direction interpretation given the possibility of post emplacement modification.

The formation of three sub-fabrics for ramp at Flow 7 further suggests the reworking of the magnetic fabrics by the subsequent lava flow below the ramp (Fig. 5). Another possible interpretation for the formation of sub-fabric is the presence of detached bands of entrained clinker between the ramps (Fig. S3). The hot lava causes the deformation of the clinker and later detaches that deformed clinker to the ramp zone (Fig. S3). This can also affect the primary magnetic fabrics of ramp. For ramp at Flow 4, the flow direction towards N obtained from AMS is consistent with the known regional flow direction of the SB lava flow field. As there is no subsequent flow underneath the ramp, we can safely eliminate the possibility of post-emplacement modification of the flow fabric (Fig. 7). The shift of the foliation plane dip from sub-horizontal to incline at the southern and northern ends of the ramp, respectively, shows the evolution of the ramp formation. Moreover, in the northern ends, the magnetic lineation dispersion on the flow plane might suggest spreading toward the open sea.

Tubes

The lava tubes observed along the coast within Flow 7 and Flow 1 are probably the down slope extension of the two 'a'ā lava channels observed in the middle lava flow field (Fig. 1a), whereas the smaller cavities described within Flow 1 and Flow 7 (Figs. 8 and 9) are incipient lava tubes. They are characterised by a central lava core, multiple accretionary layers, and a roof with stalactite formation (Fig. S4). However, close to the coast, the roof has been often eroded by wave action. Also, lava within the tube at SB underwent continue thermal erosion and downcutting (Bussey et al. 1997; Allred 1998; Kerr 2001; Fagents and Greeley 2001) which increased both foot space and headspace of the tube, respectively (Sawłowicz 2020). This process has been described at other lava flows, such as in Hawaii (Wood 1981), Mt St Helens (Kerr 2009) and California (Greeley and Baer 1971). The presence of lava tubes and the possibility of thermal erosion evidences a prolonged duration of the flowage within the tube and probably also a turbulent flow within the tube (Hulme 1973; Kerr 2001, 2009). The thickness of the inner coatings observed at the margins of the tube within Flow 1, being several cm thick, suggests a rather viscous flow (Calvari and Pinkerton 1999), probably the result of the flowage within the tube during the late stages of the eruption. In fact, the number of inner coatings reveals the life of the tube, with each coating corresponding to a phase of tube filled up, crust breakage and tube draining by ephemeral vent opening at its margins (Calvari and Pinkerton 1999).

The exposed central stream, due to the erosion of the roof, along with the accretionary layers gives an idea of the internal structure of the tube and its principal mode of formation (Fig. 8). As Peterson et al. (1994) stated, the initial step in the tube developments is channel formation, which involves the solidification of the outer boundary layer and the formation of lateral levees (Hulme 1974; Sparks et al. 1976). Acknowledging the fact that the quickly chilled magma keeps the initial flow fabrics (Cañón-Tapia and Coe 2002), we consider the sample from outer accretionary layer to infer flow sense (L1A-S3). We avoided the intermediate layers to

infer flow direction because of the possible modification of magnetic fabrics due to the formation of adjacent layers by the frequent overflow of the central stream (Peterson et al. 1994). Consequently, for the tube at Flow 1, the AMS results indicate a vertical foliation plane with southward flow direction. Looking at the magnetic fabrics, the vertical to sub-vertical foliation plane reflects an upward magma motion perpendicular to the overall flow direction. This might be due to the overflow of lava due to fluctuating lava input to form the accretionary layer.

Inflated pāhoehoe flow

Inflation of a lava flow refers to the swelling or expansion of the preformed surface crustal layer by the continuous input of lava in the middle, resulting in a pressure build-up in the flow unit (Hon et al. 1994). In the SB lava flow field, a marginal and now eroded seaward bench of inflated pāhoehoe developed to form an arcuate bench zone.

The observed inflated flow is characterised by a thin brittle layer at the surface, a viscoelastic layer underneath, a thick central core and a basal crust, as explained by Hon et al. (1994). The vertical foliation plane strikes in different directions, showing the inflation of the brittle vesicular layer to accommodate the pressure caused by the continuous lava input. The formation of inflation features, such as cleft and lobes, explained by Walker (1991), can be distinguished by the sub-horizontal and sub-vertical magnetic foliation planes, respectively. For the central current, the horizontal flow shows a coherent direction towards the sea, with the flattened ellipsoid highlighting the gravitational settling of crystals (Sangode et al. 2022).

The 'a'ā lava channel marks the initial stage of inflation. Flow stalling, followed by the continuous lava supply from the main vent, caused the onset of lava inflation, and this stage marked the formation of the thin outer brittle layer. Inflation of the first flow continued, and the brittle outer layer broke to accommodate the inflation of the viscoelastic layer (Fig. S5). Later, the viscoelastic and brittle layers broke as the influx of lava flows continued and caused the formation of the second flow (L2). Finally, the continuous pressure made small cracks on the surface crust and caused ooze out of spongy (S-type) flow lobes (Fig. S5). The same process of stalling, inflation and breakout repeated at least four times to extend the length of the system with four pāhoehoe lobes.

Spatial distribution of different lava components and implications for emplacement sequence

We use the field observations, in conjunction with physical lava characteristics such as porosity, connectivity and phenocryst type, to generate a comprehensive overview of the spatial distribution of the defined lava components along the coast. Lava entry to sea and/or ocean usually results in the radial distribution of lava like a fan, with the lava tube formed at the flow front to drain the 'a'ā flow and feed the submarine pāhoehoe lava bench (Kauahikaua et al. 1993; Jurado-Chichay et al. 1996; Mattox and Mangan 1997; Bosman et al. 2014; Di Traglia et al. 2018).

In the direction of ocean entry, the defined major components of the morphological system are organised in the sequence: channels, littoral, ramps, tubes and pāhoehoe (Fig. 14). While the porosity-connectivity distribution allowed us to associate ramps with channels, tubes are associated with the pāhoehoe. In addition, clast count allowed us to infer that the now eroded bench was dominated by vesicular pāhoehoe. The initial lava flow in the master channel was followed by the ramp formation and later the tube developed at the flow front to feed vesicle-rich pāhoehoe flow (Fig. 14).

Although the overall vesicularity of the lava depends mainly on the initial vesicle distribution, this can be modified later by various factors, including the cooling conditions (Cashman and Kauahikaua 1997). The variability in vesicle concentration within the SB lava flow field is also linked to its cooling conditions. The higher proportion of finely vesicular lava observed in the northwest lateral margin of the SB lava flow field (Flow 12) can be attributed to the rapid cooling process due to the absence of adjacent lava flows along the northwest edge of the lava delta. Instead, the presence of coarse vesicles in the central to SE lateral section of the lava is attributed to a pre-existing pāhoehoe lava flow to the right of L1 (L13—L16). Here, L1 undergoes a more gradual cooling process due to the presence of adjacent pāhoehoe lava to the east (Calvari et al. 2023), allowing sufficient time for vesicle nucleation and growth.

The spatial and temporal organisation of different components can be traced by the porosity distribution. Channels and ramps with low porosity tend to be prevalent further from the zone of lava-water interaction, whereas tubes and inflated pāhoehoe, characterised by higher porosity, occur mainly within the zone of lava-water interaction. Further, the connectivity distribution of the ramp and channel-levee shows a small dispersion compared to the tube and pāhoehoe, where connectivity ~ 1, with no dispersion, suggesting that the vesicles have sufficient time to expand and coalesce to form connected vesicles (Sahagian 1985). The lava components are thus systematically organised in the flow direction, with ramping and channels being dominant inland, tubes and littoral part at the coastline and inflated pāhoehoe off-shore (Fig. 14).

Ocean entry model

The SB lava flow field of Stromboli is a natural laboratory to study the 'a'ā lava flow entry to the sea and the associated

formation of different components. Previously, Bosman et al. (2014) documented 'a'ā lava entry from Stromboli volcano during the 2007 eruption, describing the morphological evolution of the lava delta and the dynamics of submarine 'a'ā lava flow emplacement. Unlike pāhoehoe lava, which tends to fragment upon contact with water, 'a'ā lava can intrude water and hold its structure over a considerable distance (Stevenson et al. 2012). Despite this, most studies of lava-water interaction focus on pāhoehoe lava (e.g. Moore et al. 1973; Tribble 1991; Dundas et al. 2020).

The two possible interpretations of the ocean entry model for the SB lava flow field are shown in Figure 15a and b. Model 1 is characterised by a channel-fed 'a'ā lava flow spreading at low rate that stops before the coast (Fig. 15a–i). Here, the initial sanidine-rich flow descends down the slope, and, on reaching the break-in slope, the flow slows down and the flow front stops (Fig. 15a–i). Continued magma supply to the distal section causes further lava flow inflation and thickening, along with the ramping up of subsequent pulses behind the statically inflated lava flow front. This stage marks the initiation of ramp (Fig. 15a–ii). The later lava flow is sanidine poor, and the continuous lava supply causes the flow front failure to feed the pāhoehoe bench (Fig. 15a–iii). During this period, the upper crust forms a roof over the flowing lava to facilitate closed channel flow. Later, tubes form at the flow front to feed the lava bench,

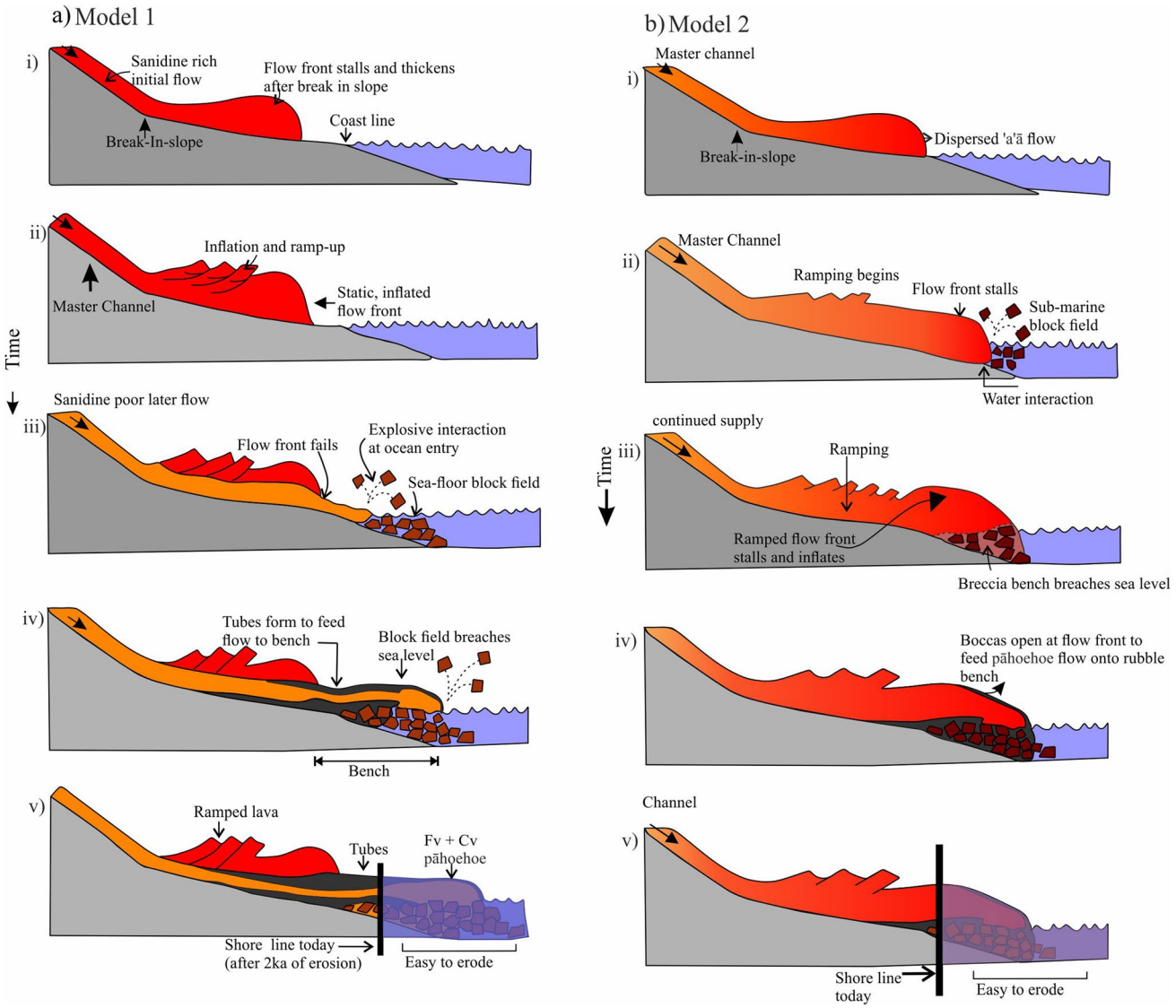

Fig. 15 Sea entry models where **a** the channel fed 'a'ā that stops before the coast and **b** the channel fed 'a'ā with a high effusion rate that crosses the coastline. Cv and Fv are coarsely and finely vesiculated pāhoehoe, respectively. In **a**, the red colour represent sanidine-rich lava, while the orange shades indicate lava with lower sanidine content. In **b**, the colour gradient illustrates the temperature gradient resulting from lava solidification

and the already developed field of blocks breaches the sea level, allowing pāhoehoe to flow without water interaction (Fig. 15a–iv). The final stage exposes the present shoreline, formed after 2–4 ka of erosion of the lava bench, comprising fine- and coarse vesicle-dominated pāhoehoe lava flows with lava tubes, and 'a'ā lava ramps behind (Fig. 15a–v).

The second interpretative model of 'a'ā lava flow entry (model 2) is characterised by a channel-fed 'a'ā with high effusion rate crossing the surface zone (Fig. 15b–i). The fast-moving lava flow on the slope begins to disperse when it encounters the break-in slope, marking the start of ramping. Meanwhile, the interaction of the 'a'ā lava with the sea water creates a submarine block field (Fig. 15bi–ii). The high effusion rate causes the formation of left bank (LB) and right bank (RB) rubble levees around the main channel as the ramping continues. The channel cuts through the surface zone, forming a submarine block field due to lava-water interaction. The continuous lava supply creates the breccia bench that accumulates at the sea level. Later, boccas open at the stalled flow front to feed the pāhoehoe flow onto the breccia bench as the lava continues to flow (Fig. 15biii–iv). Finally, erosion exposes the ramped 'a'ā lava flow with distal pāhoehoe flow lobes.

Both interpretative models can be observed at SB. Model 1 applies to channels that die out before the surf zone to feed ramped flow after the break-in-slope. Here, pāhoehoe extending from the stalled and thickened flow front move across the surf zone and tubes develop. Interaction with the water fragments the lava and results in an unstable, rubbly bench foundation, across tubes and pāhoehoe extend. This will apply to low effusion rate, and low velocity, entry into shallow water with a gently sloping offshore profile. We find that this model applies to the northern and southern sides of the entry zone.

Model 2 applies to channels extending directly across the surf zone and onwards into the water. In this case, flows are high effusion rate, and high velocity, and/or entry into deep water with a steep offshore profile. We find that model 2 applies to the central area of the entry zone and was probably the first part of the flow field to be emplaced. Instead, model 1 applies to late-stage emplacement at lower effusion rate either side of the initial entry.

Implication for lava flows in littoral settings and hazard

Thus, our multidisciplinary study allowed us to investigate the flow dynamics and emplacement mechanism of one of the most recent flank eruptions of Stromboli and to reconstruct the spatial distribution of different lava flow components. Considering the common occurrence of lava entry into water bodies, especially on volcanic islands, our model(s) serves as a reference interpretative model for such water entry of 'a'ā lava flow. Moreover, the illustration of the emplacement dynamics of each lava flow component, qualitatively assessed using the magnetic fabrics, supported by field observations, can be used for the analysis and interpretation of lava flow structures at littoral settings.

The results of our work have implications for hazard assessment in scenarios where 'a'ā lava deltas are active. The possibility of lava flow front inflation and rampart formation due to lava contact with the sea water may significantly increase the thickness of the distal lava flow field, favouring flow stacking. The sudden emptying of the inflated lava flow front to feed secondary pāhoehoe lobes and lava tube growth might cause unexpected expansion of the lava delta, as documented in other cases of basaltic and even rhyolitic flows (e.g. James et al. 2007; Applegarth et al. 2010; Tuffen et al. 2013). Our results show that the common behaviour of 'a'ā lava flows meeting the sea to granulate and feed volumetrically significant submarine gravity flows (Bosman et al. 2014; Casalbore et al. 2021) can be challenged if discharge rate is low enough to promote flow inflation and stacking (Hon et al. 1994), rather than flow expansion. This process is rather different from, and much slower than, the case when pāhoehoe flows meet the ocean, which often results in the sudden collapse of a lava delta to cause littoral explosions and the buildup of littoral cones (Mattox and Mangan 1997).

Summary

Using the sea-entry lava of Stromboli's SB eruption, we were able to define the main components of a lava delta fed by 'a'ā lava flows. There are (a) channels, (b) littoral units, (c) ramps, (d) lava tubes, and (e) inflated pāhoehoe lava flows. The spatial organisation of these components allowed us to build a descriptive model for 'a'ā lava flows entering a water body which is characterised by three main phases. The initial stage corresponds to the entry of channel-fed 'a'ā lava flow into the sea which, as in the case of pāhoehoe, fragments to form metric blocks of 'a'ā. Continued lava supply to the foreshore causes units to stall while spreading over this substrate. Subsequent 'a'ā lava flow units ramp up behind the stalled flow front barrier, creating a degassed ponded volume. Lava tubes extending through the stalled flow barrier feed the seaward extension of a pāhoehoe bench.

As in the case of Hawaii for pāhoehoe-fed benches, at Stromboli, our 'a'ā-fed bench is exceeding unstable and easy to erode, as witnessed by its erosion by wave action in the 2–4 ka since emplacement. Our model is thus one for 'a'ā lava flow arriving at a break-in-slope (from steep to shallow) at a coast, a situation which is common at many island volcanoes. Our model may thus serve as a guide for such 'a'ā lava flow water-entry conditions.

Supplementary Information The online version contains supplementary material available at https://doi.org/10.1007/s00445-024-01743-7.

Acknowledgements We are grateful to, Nina Smith and Stefan Pope, for helping us with the dive survey. We are thankful to the Stromboli guides (Magmatrek) for repatriating the cores and setting them back in place.

Funding Open access funding provided by Università degli Studi di Torino within the CRUI-CARE Agreement. This project is a part of RS PhD project. This research was funded by MIUR ex-60% attributed to EZ and PhD grants-Budget 10% attributed to RS. Also, it was partially funded by the Project FIRST (ForecastIng eRuptive activity at Stromboli volcano: Timing, eruptive style, size, intensity, and duration), INGV-Progetto Strategico Dipartimento Vulcani 2019 (Delibera n. 144/2020). This is contribution no. 637 of the ClerVolc program of the International Research Center for Disaster Sciences and Sustainable Development of the University of Clermont Auvergne.

References

Allred K (1998) Lava tube remelt by radiant heat and burning gasses. Int J Speleol 27(1):13

Alonso I, Santana-Sarmiento FJ, Andrés-Araujo F et al (2023) Morphosedimentary characteristics and formation mechanisms of new beaches generated after the Tajogaite volcano eruption of 2021 (La Palma, Spain). Mar Geol 462:107099. https://doi.org/10.1016/j.margeo.2023.107099

Applegarth LJ, Pinkerton H, James MR, Calvari S (2010) Lava flow superposition: the reactivation of flow units in compound 'a'ā flows. J Volcanol Geoth Res 194:100–106. https://doi.org/10.1016/j.jvolgeores.2010.05.001

Arrighi S, Rosi M, Tanguy J, Courtillot V (2004) Recent eruptive history of stromboli (Aeolian Islands, Italy) determined from high-accuracy archeomagnetic dating. Geophys Res Letters 31:2004GL020627. https://doi.org/10.1029/2004GL020627

Banerjee P, Shen Y (2023) Hydrovolcanic explosions at the lava ocean entry of the 2018 Kilauea eruption recorded by ocean-bottom seismometers. Seismol Res Lett. https://doi.org/10.1785/0220220195

Bosman A, Casalbore D, Romagnoli C, Chiocci FL (2014) Formation of an 'a'ā lava delta: insights from time-lapse multibeam bathymetry and direct observations during the Stromboli 2007 eruption. Bull Volcanol 76:838. https://doi.org/10.1007/s00445-014-0838-2

Bussey DBJ, Guest JE, Sørensen SA (1997) On the role of thermal conductivity on thermal erosion by lava. J Geophys Res 102:10905–10908. https://doi.org/10.1029/97JE00415

Callot JP, Guichet X (2003) Rock texture and magnetic lineation in dykes: a simple analytical model. Tectonophysics 366:207–222. https://doi.org/10.1016/S0040-1951(03)00096-9

Calvari S, Pinkerton H (1999) Lava tube morphology on Etna and evidence for lava flow emplacement mechanisms. J Volcanol Geoth Res 90:263–280. https://doi.org/10.1016/S0377-0273(99)00024-4

Calvari S, Branca S, Corsaro RA, De Beni E, Miraglia L, Norini G, Wijbrans J, Boschi E (2011) Reconstruction of the eruptive activity on the NE sector of Stromboli volcano: timing of flank eruptions since 15 ka. Bull Volcanol 73:101–112. https://doi.org/10.1007/s00445-010-0412-5

Calvari S, Marotta E, Vicari A, Famiglietti NA, Ganci G, Miraglia L, Avino R, Avvisati G, Belviso P, Bilotta G, Cappello A, D'Ambrosio C, Moschillo R, De Luca G, Memmolo A, Messina L, Minichiello F, Peluso R (2023) The San Bartolo lava flow Field along the northeast flank of Stromboli volcano: a preliminary study for field survey. https://doi.org/10.5281/zenodo.7760868

Cañón-Tapia E, Walker GPL, Herrero-Bervera E (1996) The internal structure of lava flows—insights from AMS measurements I: near-vent a'a. J Volcanol Geotherm Res 70:21–36. https://doi.org/10.1016/0377-0273(95)00050-X

Cañón-Tapia E (2004) Anisotropy of magnetic susceptibility of lava flows and dykes a historical account. Geol Soc Lond Spec Publ 238:205–225. https://doi.org/10.1144/GSL.SP.2004.238.01.14

Cañón-Tapia E, Coe R (2002) Rock magnetic evidence of inflation of a flood basalt lava flow. Bull Volcanol 64:289–302. https://doi.org/10.1007/s00445-002-0203-8

Cañón-Tapia E, Pinkerton H (2000) The anisotropy of magnetic susceptibility of lava flows: an experimental approach. J Volcanol Geoth Res 98:219–233. https://doi.org/10.1016/S0377-0273(99)00155-9

Casalbore D, Di Traglia F, Bosman A, Romagnoli C, Casagli N, Chiocci FL (2021) Submarine and subaerial morphological changes associated with the 2014 eruption at Stromboli Island. Remote Sens 13:2043. https://doi.org/10.3390/rs13112043

Cashman KV, Kauahikaua JP (1997) Reevaluation of vesicle distributions in basaltic lava flows. Geology 25:419. https://doi.org/10.1130/0091-7613(1997)025%3c0419:ROVDIB%3e2.3.CO;2

Chadima M (2006) Remasoft 3.0 a user-friendly paleomagnetic data browser and analyzer. Trav Géophysiques 27:20

Chouet B, Hamisevicz N, McGetchin TR (1974) Photoballistics of volcanic jet activity at Stromboli, Italy. J Geophys Res 79:4961–4976. https://doi.org/10.1029/JB079i032p04961

Colombier M, Wadsworth FB, Gurioli L, Scheu B, Kueppers U, Di Muro A, Dingwell DB (2017) The evolution of pore connectivity in volcanic rocks. Earth Planet Sci Lett 462:99–109. https://doi.org/10.1016/j.epsl.2017.01.011

Delcamp A, Petronis MS, Troll VR (2015) Discerning magmatic flow patterns in shallow-level basaltic dykes from the NE rift zone of Tenerife, Spain, using the anisotropy of magnetic susceptibility (AMS) technique. Geol Soc Lond Spec Publ 396:87–106. https://doi.org/10.1144/SP396.2

Di Traglia F, Nolesini T, Solari L, Ciampalini A, Frodella W, Steri D, Allotta B, Rindi A, Marini L, Monni N, Galardi E (2018) Lava delta deformation as a proxy for submarine slope instability. Earth Planet Sci Lett 488:46–58. https://doi.org/10.1016/j.epsl.2018.01.038

Dundas CM, Keszthelyi L, Lev E, Rumpf ME, Hamilton CW, Höskuldsson Á, Thordarson T (2020) Lava–water interaction and hydrothermal activity within the 2014–2015 Holuhraun lava flow field, Iceland. J Volcanol Geoth Res 408:107100. https://doi.org/10.1016/j.jvolgeores.2020.107100

Fagents S, Greeley R (2001) Factors influencing lava-substrate heat transfer and implications for thermomechanical erosion. Bull Volcanol 62:519–532. https://doi.org/10.1007/s004450000113

Fisher R (1953) Dispersion on a sphere. Proc Roy Soc A: Math Phys Eng Sci 217:295–305. https://doi.org/10.1098/rspa.1953.0064

Fitch EP, Fagents SA (2020) Characteristics of rootless cone tephra emplaced by high-energy lava–water explosions. Bull Volcanol 82:62. https://doi.org/10.1007/s00445-020-01393-5

Francalanci L, Manetti P, Peccerillo A (1989) Volcanological and magmatological evolution of Stromboli volcano (Aeolian Islands): the roles of fractional crystallization, magma mixing, crustal contamination and source heterogeneity. Bull Volcanol 51:355–378. https://doi.org/10.1007/BF01056897

Francalanci L, Lucchi F, Keller J, De Astis G, Tranne CA (2013) Chapter 13 Eruptive, volcano tectonic and magmatic history of the Stromboli volcano (north-eastern Aeolian archipelago). Memoirs 37:397–471. https://doi.org/10.1144/M37.13

Francalanci L, Braschi E, Di Salvo S, Lucchi F, Petrone CM (2014) When magmas do not interact: paired Roman-age activity revealed by tephra studies at Stromboli volcano. Bull Volcanol 76:884. https://doi.org/10.1007/s00445-014-0884-9

Greeley R, Baer R (1971) Hambone, California and its magnificent lava tubes-preliminary report. In Geol Soc Am Abstr Programs 3:128

Harris AJL, Rowland SK (2015) Lava flows and rheology. In: the encyclopedia of volcanoes 321–342

Hext GR (1963) The estimation of second-order tensors, with related tests and designs. Biometrika 50:353–373. https://doi.org/10.1093/biomet/50.3-4.353

Hon K, Kauahikaua J, Denlinger R, Mackay K (1994) Emplacement and inflation of pahoehoe sheet flows: observations and measurements of active lava flows on Kilauea Volcano Hawaii. Geol Soc Am Bull 106:351–370. https://doi.org/10.1130/0016-7606(1994)106%3c0351:EAIOPS%3e2.3.CO;2

Houghton BF, Wilson CJN (1989) A vesicularity index for pyroclastic deposits. Bull Volcanol 51:451–462. https://doi.org/10.1007/BF01078811

Hulme G (1973) Turbulent lava flow and the formation of lunar sinuous rilles. Mod Geol 4:107–117

Hulme G (1974) The interpretation of lava flow morphology. Geophys J Int 39:361–383. https://doi.org/10.1111/j.1365-246X.1974.tb05460.x

James MR, Pinkerton H, Robson S (2007) Image-based measurement of flux variation in distal regions of active lava flows. Geochem Geophys Geosyst 8:2006GC00448. https://doi.org/10.1029/2006GC001448

Jenks MD, Bonnichsen B, Chamberlain VE (1989) Subaqueous basalt eruptions into Pliocene Lake Idaho, Snake River Plain, Idaho. Guideb Geol North West Ida Surrounding Area: Ida Geol Surv Bull 28:17–34

Jurado-Chichay Z, Rowland SK, Walker GPL (1996) The formation of circular littoral cones from tube-fed pāhoehoe: Mauna Loa, Hawai'i. Bull Volcanol 57:471–482. https://doi.org/10.1007/BF00304433

Kauahikaua J, Denlinger R, Foster J, Keszthelyi L (1993) Lava delta instability: is it mass-wasting or is it triggered by lava flowing through tubes. Eos Trans 74:616

Kerr RC (2001) Thermal erosion by laminar lava flows. J Geophys Res 106:26453–26465. https://doi.org/10.1029/2001JB000227

Kerr RC (2009) Thermal erosion of felsic ground by the laminar flow of a basaltic lava, with application to the Cave Basalt, Mount St. Helens Washington. J Geophys Res 114:2009JB006430. https://doi.org/10.1029/2009JB006430

Kirschvink JL (1980) The least-squares line and plane and the analysis of palaeomagnetic data. Geophys J Int 62:699–718. https://doi.org/10.1111/j.1365-246X.1980.tb02601.x

Laiolo M, Cigolini C (2006) Mafic and ultramafic xenoliths in San Bartolo lava field: new insights on the ascent and storage of Stromboli magmas. Bull Volcanol 68:653–670. https://doi.org/10.1007/s00445-005-0040-7

Lambeck K, Antonioli F, Purcell A, Silenzi S (2004) Sea-level change along the Italian coast for the past 10,000yr. Quatern Sci Rev 23:1567–1598. https://doi.org/10.1016/j.quascirev.2004.02.009

Lipman PW, Banks NG (1987) A'a flow dynamics, 1984 Mauna Loa eruption. US Geol Surv Prof Pap 1350:1527–1567

Lodato L, Spampinato L, Harris A, Calvari S, Dehn J, Patrick M (2007) The morphology and evolution of the Stromboli 2002–2003 lava flow field: an example of a basaltic flow field emplaced on a steep slope. Bull Volcanol 69:661–679. https://doi.org/10.1007/s00445-006-0101-6

Loock S, Diot H, Van Wyk De Vries B et al (2008) Lava flow internal structure found from AMS and textural data: an example in methodology from the Chaîne des Puys, France. J Volcanol Geotherm Res 177:1092–1104. https://doi.org/10.1016/j.jvolgeores.2008.08.017

Macdonald GA (1972) Composite lava flows on Haleakala Volcano Hawaii. Geol Soc America Bull 83:2971. https://doi.org/10.1130/0016-7606(1972)83[2971:CLFOHV]2.0.CO;2

Maeno F, Taniguchi H (2006) Silicic lava dome growth in the 1934–1935 Showa Iwo-jima eruption, Kikai caldera, south of Kyushu, Japan. Bull Volcanol 68:673–688. https://doi.org/10.1007/s00445-005-0042-5

Maeno F, Nakada S, Kaneko T (2016) Morphological evolution of a new volcanic islet sustained by compound lava flows. Geology 44:259–262. https://doi.org/10.1130/G37461.1

Marsella M, Baldi P, Coltelli M, Fabris M (2012) The morphological evolution of the Sciara del Fuoco since 1868: reconstructing the effusive activity at Stromboli volcano. Bull Volcanol 74:231–248. https://doi.org/10.1007/s00445-011-0516-6

Mattox TN, Mangan MT (1997) Littoral hydrovolcanic explosions: a case study of lava–seawater interaction at Kilauea Volcano. J Volcanol Geoth Res 75:1–17. https://doi.org/10.1016/S0377-0273(96)00048-0

Mattox TN, Heliker C, Kauahikaua J, Hon K (1993) Development of the 1990 Kalapana flow field, Kilauea Volcano Hawaii. Bull Volcanol 55:407–413

Moore JG, Phillips RL, Grigg RW, Peterson DW, Swanson DA (1973) Flow of lava into the sea, 1969–1971, Kilauea Volcano Hawaii. Geol Soc Am Bull 84:537. https://doi.org/10.1130/0016-7606(1973)84%3c537:FOLITS%3e2.0.CO;2

Mueller WU, Garde AA, Stendal H (2000) Shallow-water, eruption-fed, mafic pyroclastic deposits along a Paleoproterozoic coastline: Kangerluluk volcano-sedimentary sequence, southeast Greenland. Precambr Res 101:163–192. https://doi.org/10.1016/S0301-9268(99)00087-X

Mulas M, Cioni R, Andronico D, Mundula F (2016) The explosive activity of the 1669 Monti Rossi eruption at Mt. Etna (Italy). J Volcanol Geoth Res 328:115–133. https://doi.org/10.1016/j.jvolgeores.2016.10.012

Obata S, Umino S (1999) Morphology of AD 864 Aokigahara lava flow exposed on the coast of Motosuko lake Fuji Volcano. Kazan 44(4):201–216

Olšanská I, Tomek F, Chadima M et al (2024) Magnetic multi-fabrics as tools for understanding ignimbrite emplacement processes: an example from late-Variscan Tharandter Wald Caldera, Bohemian Massif. J Struct Geol 178:105012. https://doi.org/10.1016/j.jsg.2023.105012

Patrick MR, Harris AJL, Ripepe M et al (2007) Strombolian explosive styles and source conditions: insights from thermal (FLIR) video. Bull Volcanol 69:769–784. https://doi.org/10.1007/s00445-006-0107-0

Peccerillo A, Taylor SR (1976) Geochemistry of eocene calc-alkaline volcanic rocks from the Kastamonu area, Northern Turkey. Contr Mineral Petrol 58:63–81. https://doi.org/10.1007/BF00384745

Peterson DW, Holcomb RT, Tilling RI, Christiansen RL (1994) Development of lava tubes in the light of observations at Mauna Ulu, Kilauea Volcano Hawaii. Bull Volcanol 56:343–360. https://doi.org/10.1007/BF00326461

Poland MP, Orr TR (2014) Identifying hazards associated with lava deltas. Bull Volcanol 76:880. https://doi.org/10.1007/s00445-014-0880-0

Prival J-M, Harris AJL, Zanella E et al (2022) Emplacement dynamics of a crystal-rich, highly viscous trachytic flow of the Sancy stratovolcano, France. GSA Bull. https://doi.org/10.1130/B36415.1

Romagnoli C (2013) Chapter 3 characteristics and morphological evolution of the Aeolian volcanoes from the study of submarine portions. Memoirs 37:13–26. https://doi.org/10.1144/M37.3

Rosi M, Bertagnini A, Landi P (2000) Onset of the persistent activity at Stromboli volcano (Italy). Bull Volcanol 62:294–300. https://doi.org/10.1007/s004450000098

Sahagian D (1985) Bubble migration and coalescence during the solidification of basaltic lava flows. J Geol 93:205–211. https://doi.org/10.1086/628942

Sangode SJ, Tembhurne S, Mahajan R, Deenadayalan K, Meshram DC, Dongre AN, Bhagat AR, Satyanarayana KVV (2022) Magnetic fabrics and magnetic mineralogical variations in lava channel: an example from the Deccan volcanic province India. J Earth Syst Sci 131:24. https://doi.org/10.1007/s12040-021-01769-x

Sawłowicz Z (2020) A short review of pyroducts (lava tubes). ASGP. https://doi.org/10.14241/asgp.2020.34

Sheridan MF, Wohletz KH (1983) Hydrovolcanism: basic considerations and review. J Volcanol Geoth Res 17:1–29. https://doi.org/10.1016/0377-0273(83)90060-4

Skilling IP (2002) Basaltic pahoehoe lava-fed deltas: large-scale characteristics, clast generation, emplacement processes and environmental discrimination. Geol Soc Lond Spec Publ 202:91–113. https://doi.org/10.1144/GSL.SP.2002.202.01.06

Soule SA, Zoeller M, Parcheta C (2021) Submarine lava deltas of the 2018 eruption of Kīlauea volcano. Bull Volcanol 83:23. https://doi.org/10.1007/s00445-020-01424-1

Sparks RSJ, Pinkerton H, Hulme G (1976) Classification and formation of lava levees on Mount Etna Sicily. Geol 4:269. https://doi.org/10.1130/0091-7613(1976)4%3c269:CAFOLL%3e2.0.CO;2

Speranza F, Pompilio M, D'Ajello Caracciolo F, Sagnotti L (2008) Holocene eruptive history of the Stromboli volcano: constraints from paleomagnetic dating. J Geophys Res 113:B09101. https://doi.org/10.1029/2007JB005139

Staudacher T, Ferrazzini V, Peltier A, Kowalski P, Boissier P, Catherine P, Lauret F, Massin F (2009) The April 2007 eruption and the Dolomieu crater collapse, two major events at Piton de la Fournaise (La Réunion Island, Indian Ocean). J Volcanol Geoth Res 184:126–137. https://doi.org/10.1016/j.jvolgeores.2008.11.005

Stevenson JA, Mitchell NC, Mochrie F, Cassidy M, Pinkerton H (2012) Lava penetrating water: the different behaviours of pāhoehoe and 'a'ā at the Nesjahraun, Þingvellir, Iceland. Bull Volcanol 74:33–46. https://doi.org/10.1007/s00445-011-0480-1

Tarling D, Hrouda F (eds) (1993) Magnetic anisotropy of rocks. Springer Science & Business Media

Thivet S, Gurioli L, Di Muro A (2020) Basaltic dyke eruptions at Piton de La Fournaise: characterization of the eruptive products with implications for reservoir conditions, conduit processes and eruptive dynamics. Contrib Mineral Petrol 175:26. https://doi.org/10.1007/s00410-020-1664-5

Tribble GW (1991) Underwater observations of active lava flows from Kilauea volcano Hawaii. Geology 19:633. https://doi.org/10.1130/0091-7613(1991)019%3c0633:UOOALF%3e2.3.CO;2

Tucker DS, Scott KM (2009) Structures and facies associated with the flow of subaerial basaltic lava into a deep freshwater lake: the Sulphur Creek lava flow, North Cascades, Washington. J Volcanol Geoth Res 185:311–322. https://doi.org/10.1016/j.jvolgeores.2008.11.028

Tuffen H, James MR, Castro JM, Schipper CI (2013) Exceptional mobility of an advancing rhyolitic obsidian flow at Cordón Caulle volcano in Chile. Nat Commun 4:2709. https://doi.org/10.1038/ncomms3709

Van der Plas L, Tobi AC (1965) A chart for judging the reliability of point counting results. Am J Sci 263(1):87–90. https://doi.org/10.2475/ajs.263.1.87

Walker GPL (1991) Structure, and origin by injection of lava under surface crust, of tumuli, "'lava rises'', "'lava-rise pits'', and "'lava-inflation clefts'' in Hawaii. Bull Volcanol 53:546–558. https://doi.org/10.1007/BF00298155

Wood C (1981) Exploration and geology of some lava tube caves on the Hawaiian volcanoes. Trans British Cave Res Assoc 8:111–129

Zijderveld JDA (1967) The natural remanent magnetizations of the exeter volcanic traps (Permian, Europe). Tectonophysics 4:121–153. https://doi.org/10.1016/0040-1951(67)90048-0